Electronic Supplementary Information

Intrinsic Reversibility in Ir-based Electrocatalysts via Dynamic Segregated-Surface Reconstruction

Sang-Hoon You[a†], Hyeonjung Jung[b†], Kyu-Su Kim[a,c], Jinwoo Baek[a], Gogwon Choe[a], Jaekyung Yi[d], Sang-Mun Jung[a], Ki-Jeong Kim[e], Sarah S. Park[d], Jeong Woo Han[b*], Kug-Seung Lee[e*] and Yong-Tae Kim[a*]

[a]Department of Materials Science and Engineering, Pohang University of Science and Technology, Gyeongbuk 37673, Republic of Korea

[b]Department of Materials Science and Engineering, Research Institute of Advanced Materials, Seoul National University (SNU), Seoul 08826, Republic of Korea

[c]Department of Mechanical Engineering, Dong-A University (DAU), Busan 49315, Republic of Korea

[d]Department of Chemistry, Pohang University of Science and Technology (POSTECH), Pohang 37673, Republic of Korea

[e]Pohang Accelerator Laboratory, Pohang University of Science and Technology, Pohang, 37673 Republic of Korea

†These authors contributed equally to this work.

*E-mail: *yongtae@postech.ac.kr, lks3006@postech.ac.kr, jwhan98@snu.ac.kr*

Table of Contents

Page

Electrochemical Screening of Ir–TM Alloy Model Catalysts

We first selected 3d-transition metals (TMs), Mn, Fe, Co, and Ni, as alloy candidates and fabricated model catalysts (Ir-TM/Ir) by annealing each TM precursor with an Ir precursor on a clean polycrystalline Ir pellet. By sequentially measuring HER-OER-HOR to determine the maximum activity for each electrochemical reaction (**Figure S1–6**), and further applying a small current (1 mA/cm^2) for 100 min to simulate gradual oxidation under realistic operating conditions (**Figure S1d–6d**), we compared how effectively reversible behavior was maintained during repeated oxidation cycles. Additionally, for a fair comparison, we conducted the same experiments under identical conditions using Ir and Pt precursors as well as bare Ir.

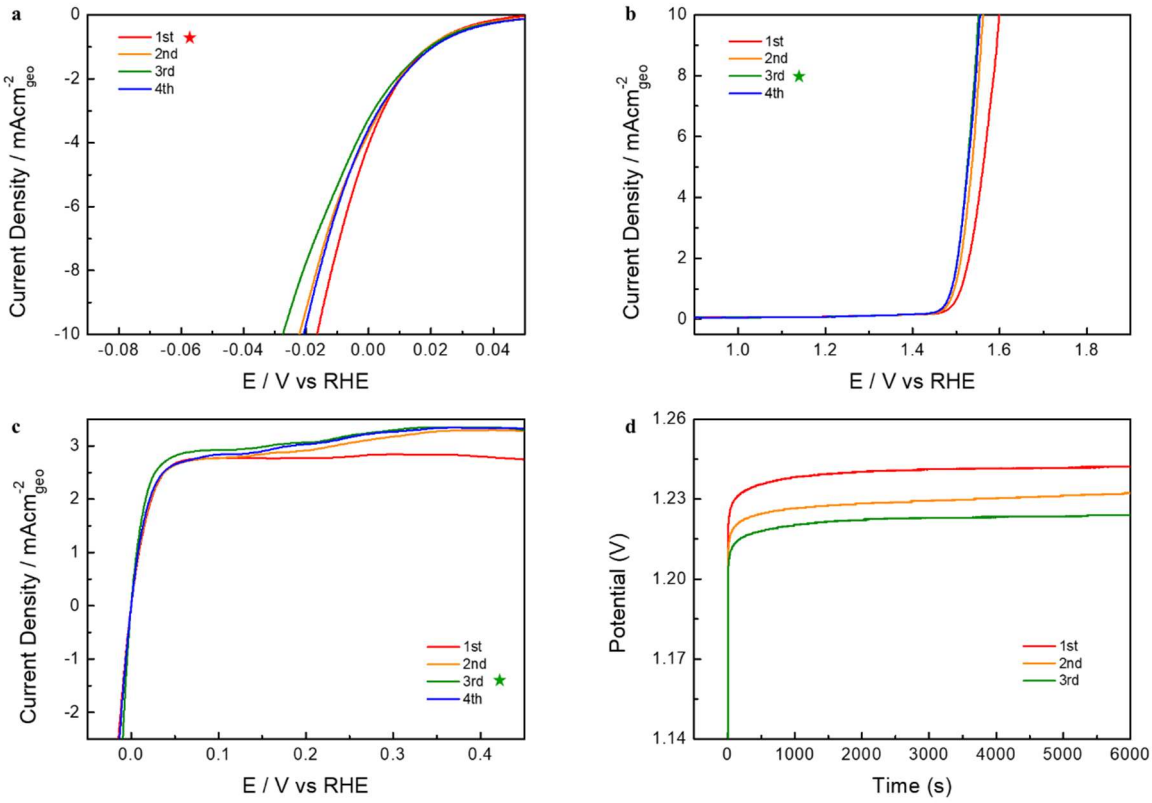

Figure S1. Sequential HER–OER–HOR polarization curves of Ir–Mn/Ir each over repeated redox cycles and long-term oxidation protocol. (a) hydrogen evolution reaction polarization curves in Ar-purged 0.1 M $HClO_4$, **(b)** oxygen evolution reaction polarization curves in Ar-purged 0.1 M $HClO_4$, **(c)** hydrogen oxidation reaction polarization curves in H_2-purged 0.1 M $HClO_4$ at 1,600 rpm with a sweep rate of 10 mVs^{-1}. **(d)** Chronopotentiometry response in Ar-purged 0.1 M $HClO_4$ at 1 mA/cm² for 100 min.

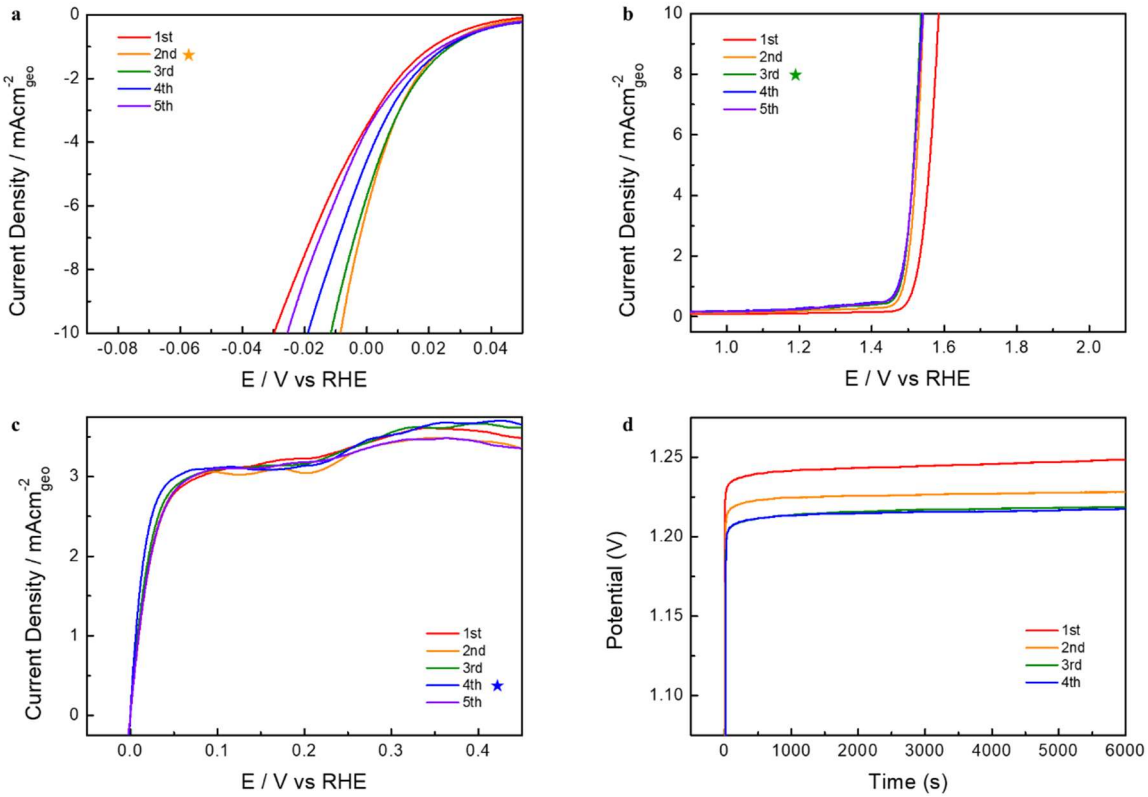

Figure S2. Sequential HER–OER–HOR polarization curves of Ir–Fe/Ir each over repeated redox cycles and long-term oxidation protocol. (a) hydrogen evolution reaction polarization curves in Ar-purged 0.1 M $HClO_4$, **(b)** oxygen evolution reaction polarization curves in Ar-purged 0.1 M $HClO_4$, **(c)** hydrogen oxidation reaction polarization curves in H_2-purged 0.1 M $HClO_4$ at 1,600 rpm with a sweep rate of 10 mVs^{-1}. **(d)** Chronopotentiometry response in Ar-purged 0.1 M $HClO_4$ at 1 mA/cm² for 100 min.

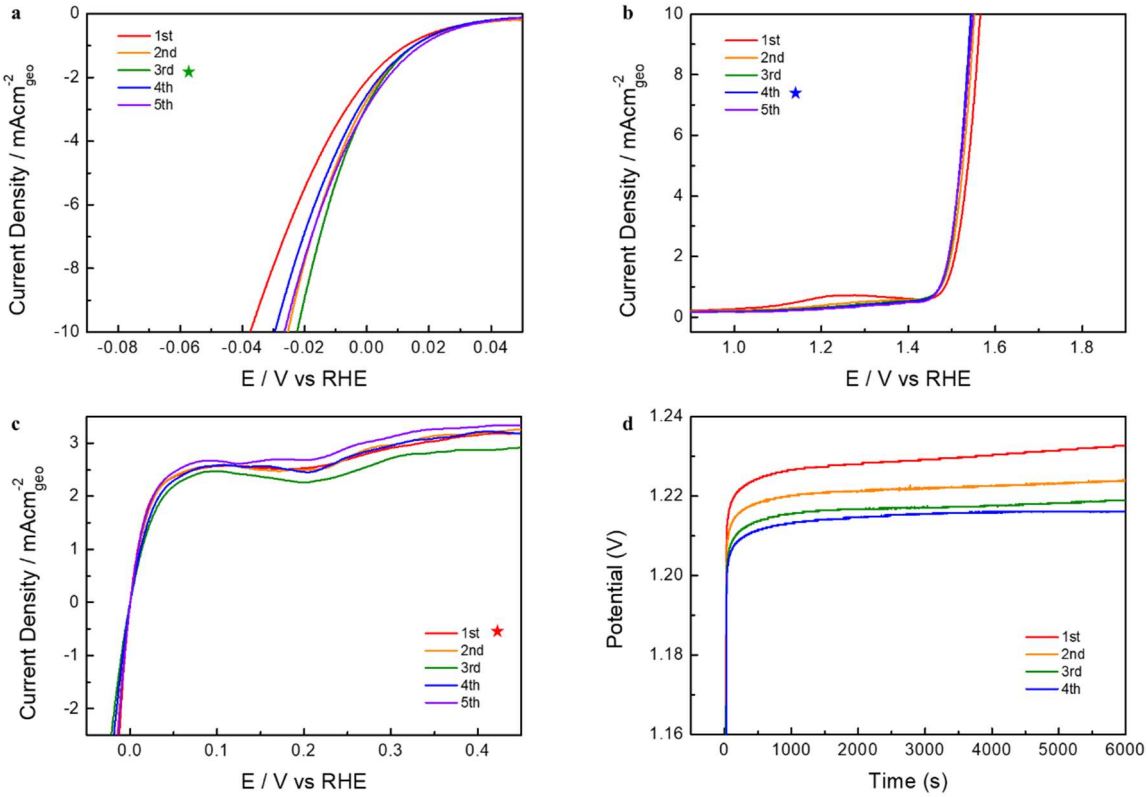

Figure S3. Sequential HER–OER–HOR polarization curves of Ir–Co/Ir each over repeated redox cycles and long-term oxidation protocol. (a) hydrogen evolution reaction polarization curves in Ar-purged 0.1 M $HClO_4$, **(b)** oxygen evolution reaction polarization curves in Ar-purged 0.1 M $HClO_4$, **(c)** hydrogen oxidation reaction polarization curves in H_2-purged 0.1 M $HClO_4$ at 1,600 rpm with a sweep rate of 10 mVs^{-1}. **(d)** Chronopotentiometry response in Ar-purged 0.1 M $HClO_4$ at 1 mA/cm² for 100 min.

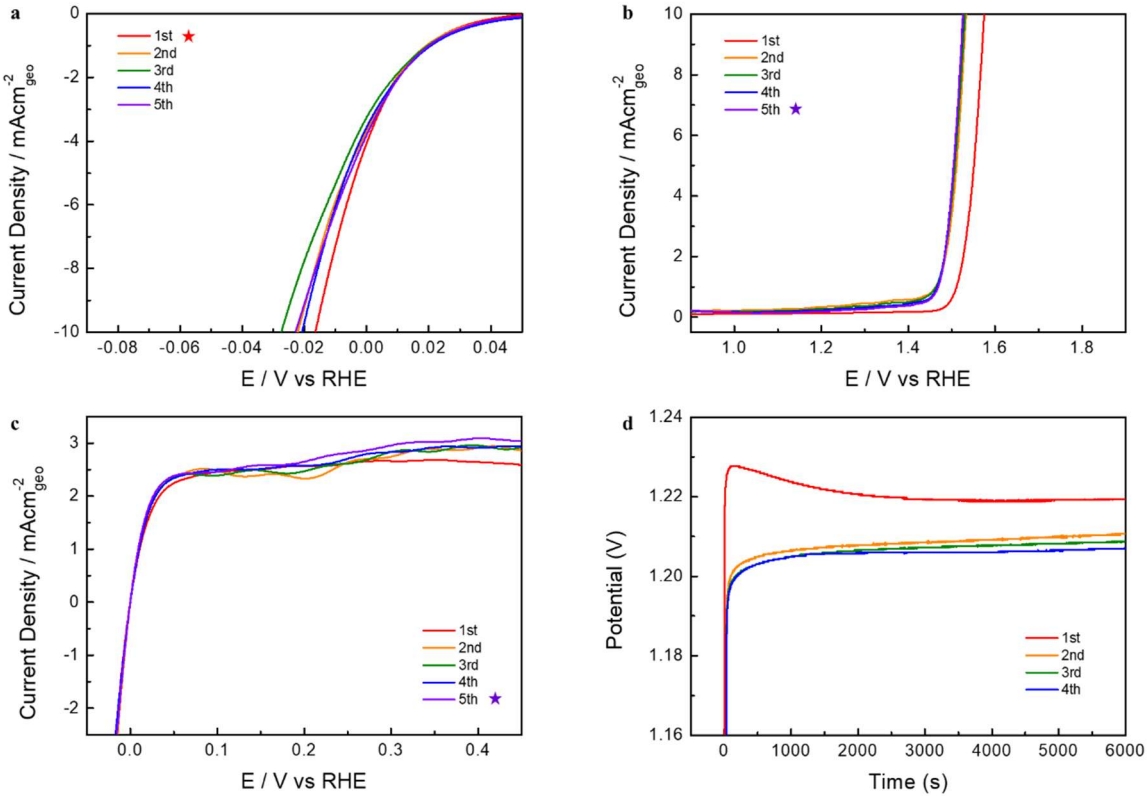

Figure S4. Sequential HER–OER–HOR polarization curves of Ir–Ni/Ir each over repeated redox cycles and long-term oxidation protocol. (a) hydrogen evolution reaction polarization curves in Ar-purged 0.1 M $HClO_4$, **(b)** oxygen evolution reaction polarization curves in Ar-purged 0.1 M $HClO_4$, **(c)** hydrogen oxidation reaction polarization curves in H_2-purged 0.1 M $HClO_4$ at 1,600 rpm with a sweep rate of 10 mVs^{-1}. **(d)** Chronopotentiometry response in Ar-purged 0.1 M $HClO_4$ at 1 mA/cm² for 100 min.

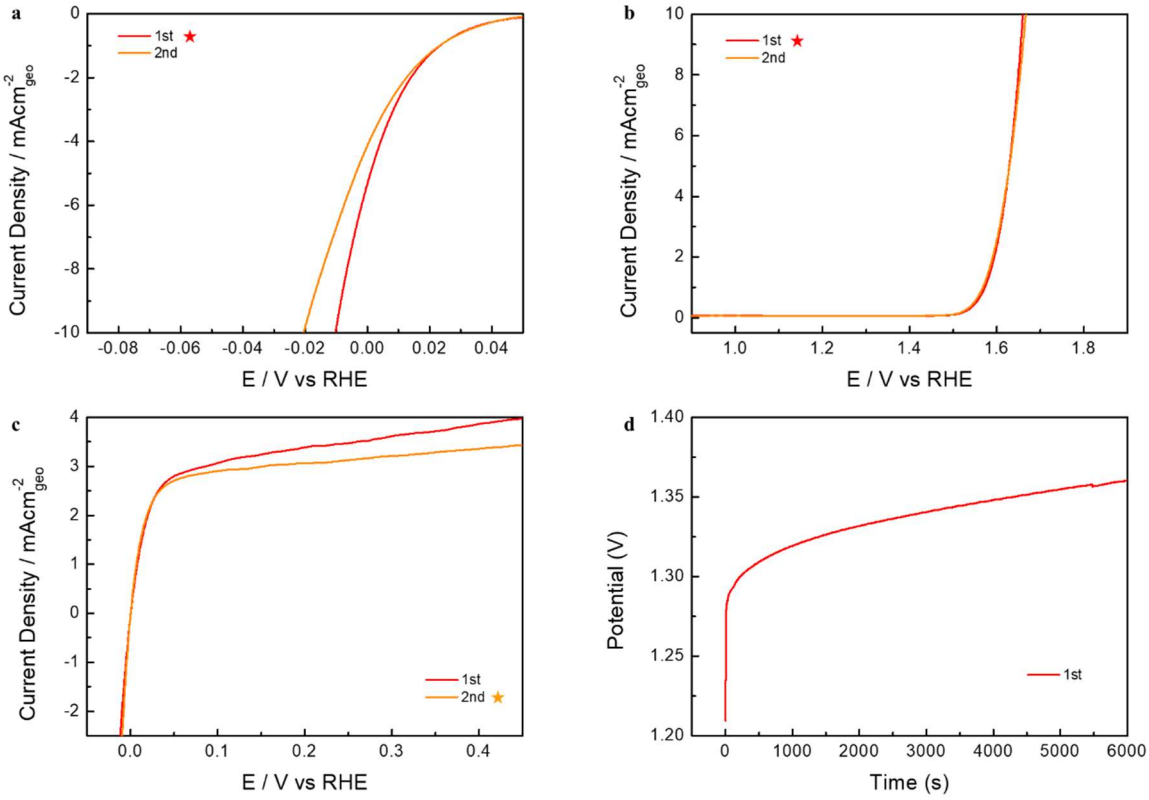

Figure S5. Sequential HER–OER–HOR polarization curves of Ir/Ir each over repeated redox cycles and long-term oxidation protocol. (a) hydrogen evolution reaction polarization curves in Ar-purged 0.1 M $HClO_4$, **(b)** oxygen evolution reaction polarization curves in Ar-purged 0.1 M $HClO_4$, **(c)** hydrogen oxidation reaction polarization curves in H_2-purged 0.1 M $HClO_4$ at 1,600 rpm with a sweep rate of 10 mVs^{-1}. **(d)** Chronopotentiometry response in Ar-purged 0.1 M $HClO_4$ at 1 mA/cm² for 100 min.

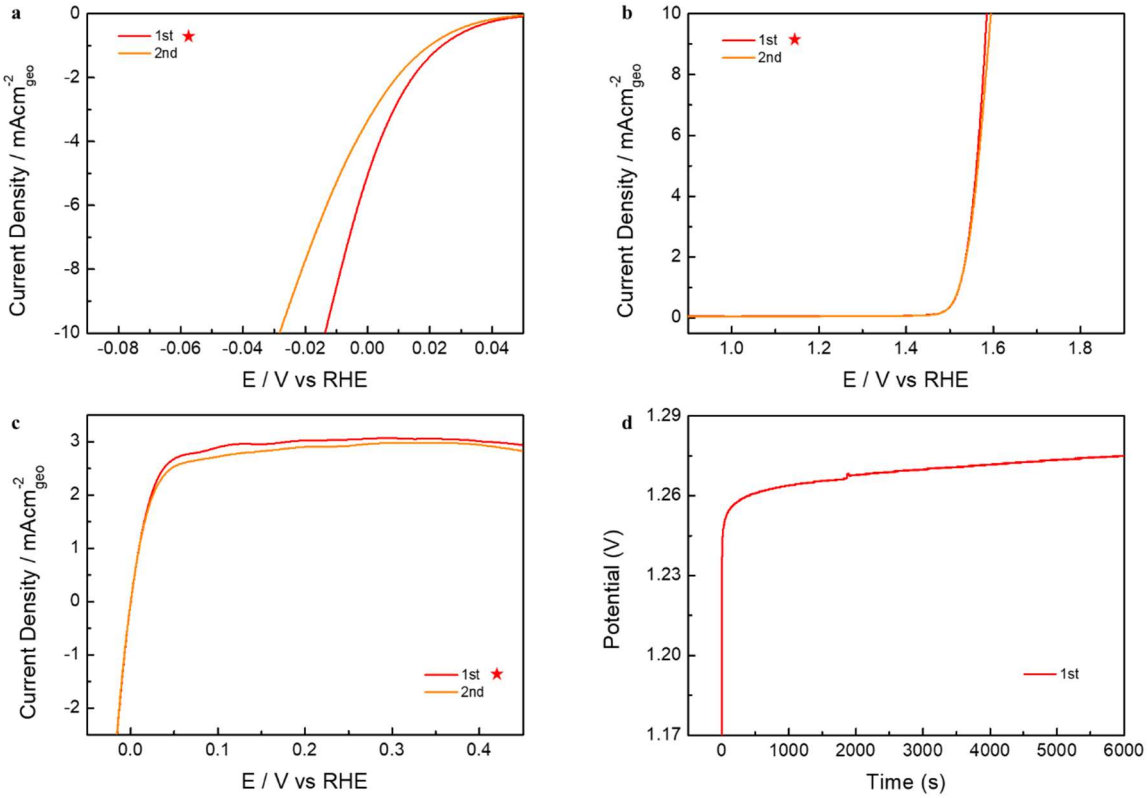

Figure S6. Sequential HER–OER–HOR polarization curves of Pt/Ir each over repeated redox cycles and long-term oxidation protocol. (a) hydrogen evolution reaction polarization curves in Ar-purged 0.1 M $HClO_4$, **(b)** oxygen evolution reaction polarization curves in Ar-purged 0.1 M $HClO_4$, **(c)** hydrogen oxidation reaction polarization curves in H_2-purged 0.1 M $HClO_4$ at 1,600 rpm with a sweep rate of 10 mVs^{-1}. **(d)** Chronopotentiometry response in Ar-purged 0.1 M $HClO_4$ at 1 mA/cm² for 100 min.

Through this electrochemical material screening, we aimed to evaluate the potential for reversible catalyst behavior by examining changes in catalytic activity over the experimental cycles. First, to assess the maximum catalytic activity achieved through multiple reaction cycles, we extracted the polarization curves representing peak activity for each reaction in the comparison groups and overlaid them in a single graph (**Figure S7a–c**). In **Figure S7a**, HER activity is compared based on the overpotential (@–10 mA/cm^2) as follows: Ir-Fe/Ir (8.5 mV) > Pt/Ir (10.3 mV) > Ir/Ir (12.3 mV) > Ir-Ni/Ir (16.5 mV) > Ir-Mn/Ir (21.5 mV) > Ir-Co/Ir (22.4 mV) > Bare Ir (43.9 mV). Similarly, the OER performance based on overpotential (@10 mA/cm^2) (**Figure S7b**) shows the following trend: Ir-Co/Ir (290 mV) > Ir-Ni/Ir (295 mV) > Ir-Fe/Ir (305 mV) > Ir-Mn/Ir (321 mV) > Ir/Ir (351 mV) > Bare Ir (419 mV) > Pt/Ir (430 mV). Lastly, HOR activity was compared using the half-wave potential (**Figure S7c**), showing the following order of increasing activity: Ir-Fe/Ir (10.2 mV) > Ir-Mn/Ir (10.7 mV) > Pt/Ir (11.4 mV) > Ir/Ir (14.0 mV) > Ir-Co/Ir (15.6 mV) > Ir-Ni/Ir (15.7 mV) > Bare Ir (17.6 mV). These results indicate that the Ir-Fe alloy delivers the highest activity for HER and HOR, while also exhibiting excellent OER performance. Next, we examined the consistency of electrochemical performance under optimal surface activation states to identify which catalyst maintained uniformly high activity across different reactions. Therefore, for each Ir-TM (TM: Mn, Fe, Co, Ni) alloy, we selected the optimal activation cycle and compared the corresponding polarization curves comprehensively (**Figure S7d–f**). Specifically, we determined that Ir-Mn in the 4th cycle, Ir-Fe in the 3rd cycle, Ir-Co in the 2nd cycle, and Ir-Ni in the 4th cycle exhibited overall high activity across all three reactions. As a result, the HER activity trend was: Pt/Ir (10.3 mV) > Ir-Fe/Ir (11.2 mV) > Ir/Ir (12.3 mV) > Ir-Mn/Ir (20.9 mV) > Ir-Ni/Ir (22.1 mV) > Ir-Co/Ir (25.2 mV) > Bare Ir (43.9 mV) (**Figure S7d**); OER: Ir-Ni/Ir (296 mV) > Ir-Fe/Ir (305 mV) > Ir-Co/Ir (320 mV) > Ir-Mn/Ir (323 mV) > Ir/Ir (351 mV) > Bare Ir (419 mV) > Pt/Ir (430 mV) (**Figure S7e**); and HOR: Ir-Mn/Ir (13.5 mV) > Ir-Fe/Ir (13.9 mV) > Pt/Ir (11.4 mV) > Ir/Ir (14.0 mV) > Ir-Co/Ir (17.1 mV) > Ir-Ni/Ir (17.3 mV) > Bare Ir (17.6 mV) (**Figure S7f**). These results also confirm that the Ir-Fe alloy exhibits the most uniformly high activity across HER, OER, and HOR. Considering **Figure S1–7** comprehensively, we selected the Ir-Fe alloy as the most suitable catalyst material in this study, as it consistently maintains excellent and uniform activity across HER, OER, and HOR, even though somewhat stochastic activation processes.

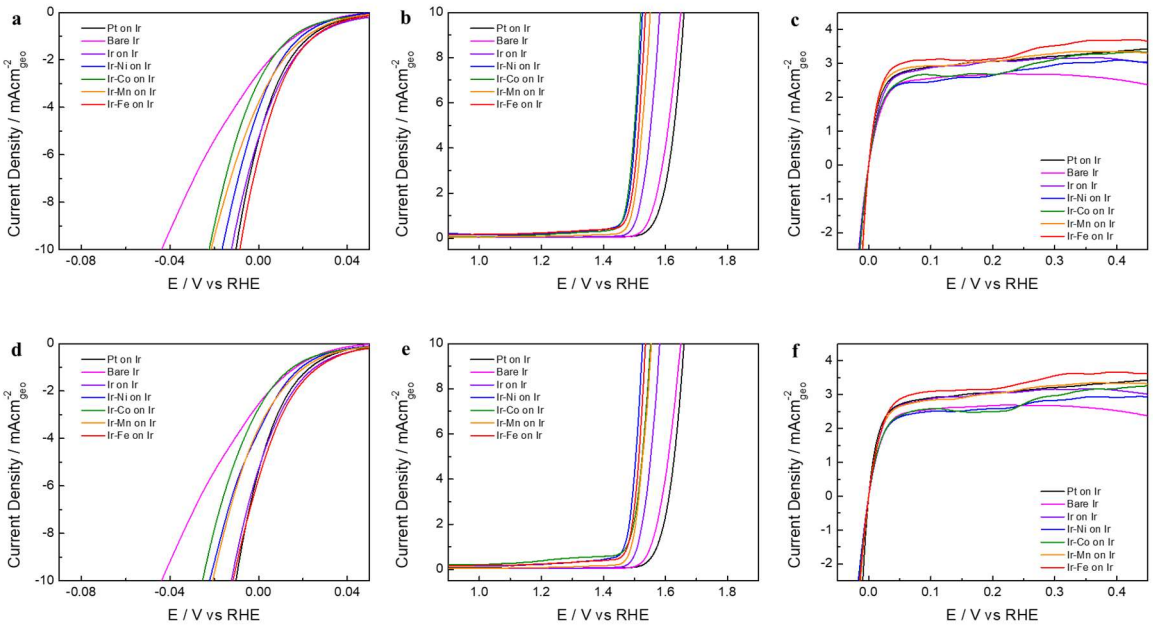

Figure S7. (a–c) Comparison of HER, OER, and HOR activities across different Ir–TM/Ir model catalysts based on peak performance. **(d–f)** Optimal cycle-based performance for each Ir–TM/Ir, highlighting stable electrochemical behavior. Ir–Fe/Ir exhibits the most uniform and superior activity across all three reactions.

Synthesis of IrFe/C Nanoparticles and Optimization Composition

While model catalysts using polycrystalline Ir pellets and metal precursors are useful for simple activity comparisons, they are unsuitable for detailed analysis or scale-up applications like unit cell testing. Therefore, we synthesized IrFe/C catalyst nanoparticles by supporting the Ir-Fe alloy on carbon black and investigated the optimal Ir to Fe molar ratio. In **Figure S8**, all samples show typical X-ray diffraction (XRD) patterns of a cubic ($Fm\bar{3}m$) system. The shift of the enlarged (111) peak toward Fe with an increasing Fe/Ir ratio, without significant peak splitting, suggests the formation of an Ir-Fe solid solution alloy. The intensity of iron oxide impurity peaks increases with the Fe/Ir ratio, and once it exceeds 5, the (111) peak no longer shifts to higher angles, indicating Fe saturation within the alloy. Excess Fe precipitates as iron oxide. Subsequent HER, OER, and HOR measurements showed the best activity when the Fe/Ir ratio increased from 1 to 3, followed by a decline as the ratio increased to 5 and 10 (**Figure S9**). We concluded that Ir:Fe = 1:3 is the optimal molar ratio, and all subsequent experiments used IrFe/C with this composition.

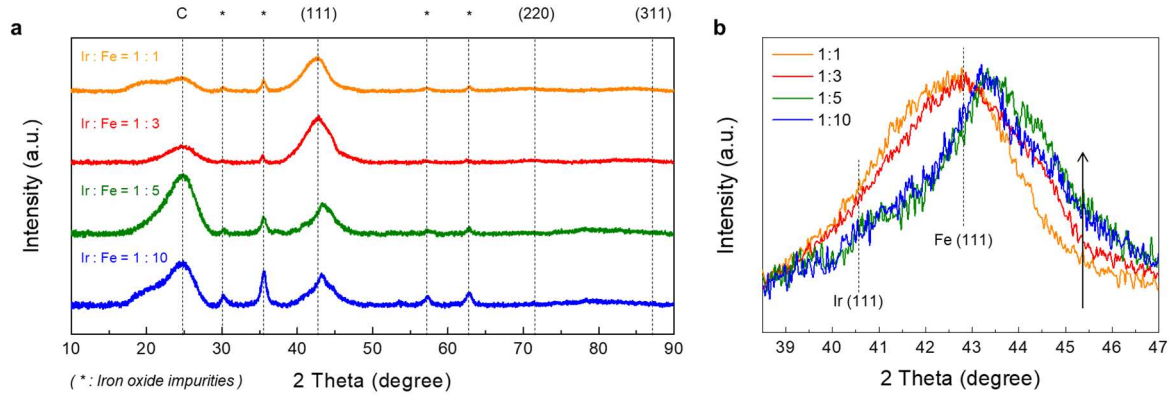

Figure S8. X-ray diffraction patterns of IrFe/C nanoparticles with varying Ir:Fe molar ratios. (a) XRD patterns of catalysis with different Fe/Ir ratios of 1, 3, 5, and 10. The peaks corresponding to iron oxide impurities are marked with *, and the broad peak around 25° from the carbon substrate is marked with C. **(b)** Enlarged (111) peak of the catalysis. The peaks have been normalized for better comparison.

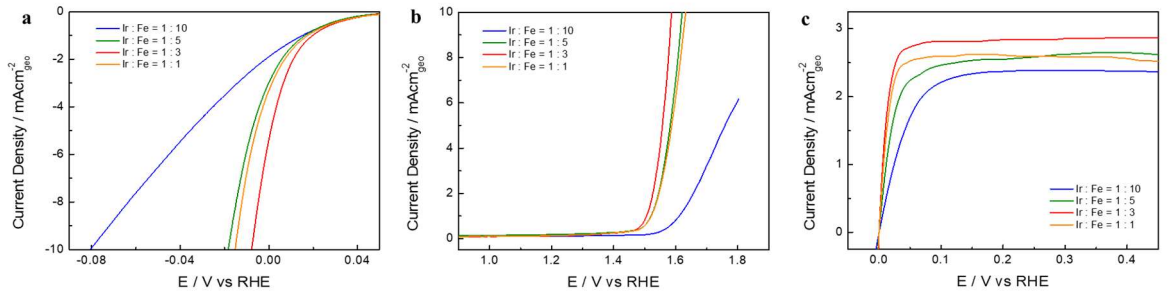

Figure S9. HER, OER, and HOR polarization curves of IrFe/C with different Ir:Fe ratios. The Ir:Fe = 1:3 composition exhibits the best performance across all reactions. **(a)** hydrogen evolution reaction polarization curves in Ar-purged 0.1 M $HClO_4$, **(b)** oxygen evolution reaction polarization curves in Ar-purged 0.1 M $HClO_4$, **(c)** hydrogen oxidation reaction polarization curves in H_2-purged 0.1 M $HClO_4$ at 1,600 rpm with a sweep rate of 10 mVs^{-1}.

Structural Characterization of Optimized IrFe/C Nanoparticles

To obtain further crystallographic information about the IrFe/C nanoparticles, we performed Rietveld refinement on the powder diffraction data (**Figure S10**). The lattice parameters of pure Fe and Ir are 3.66 and 3.85 Å, respectively. The lattice parameter of the Fe/Ir = 3 catalyst closely matching that of Fe confirms that this catalyst forms a Fe-rich Ir-Fe solid solution alloy. We examined the microstructure and crystallographic characteristics of the IrFe/C nanoparticles using high-resolution transmission electron microscopy (HR-TEM) and energy-dispersive X-ray spectroscopy (EDS)-based elemental mapping. In **Figure S11**, Ir-Fe clusters of 5–10 nm are highly dispersed and well-supported on carbon black particles of 50 to 100 nm. As shown in **Figure S12**, the consistent detection of both Ir and Fe at the same locations with uniform intensity suggests that Ir and Fe co-exist in alloy form, consistent with the XRD results.

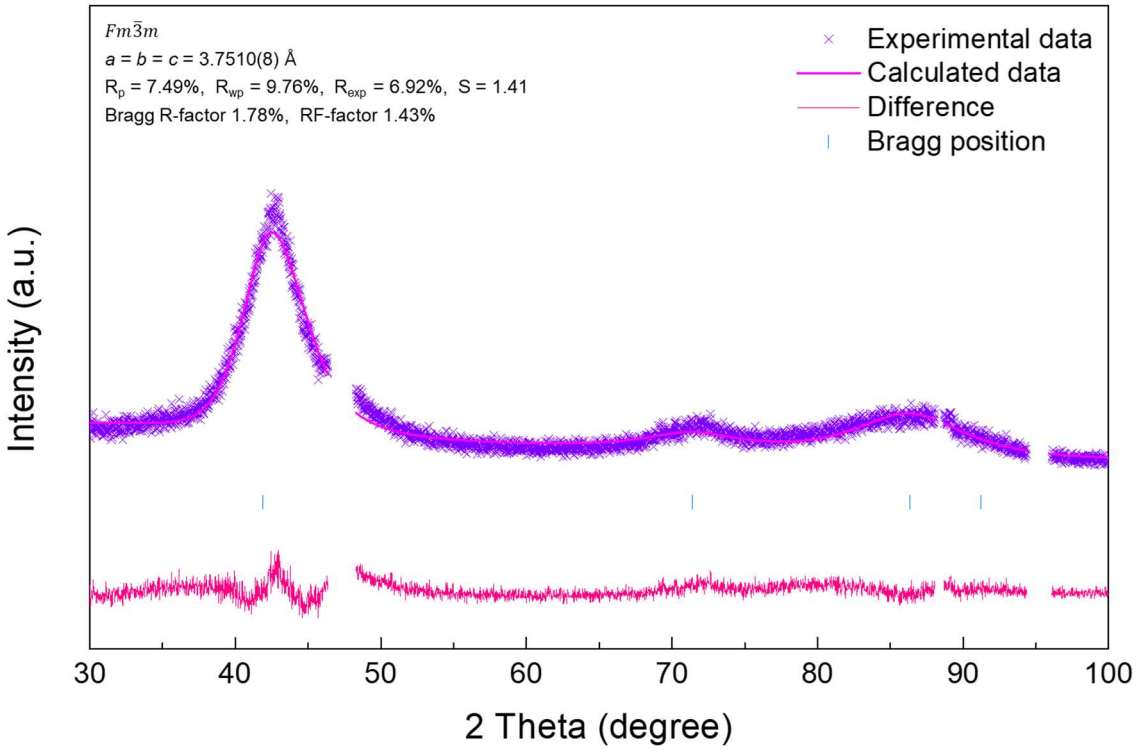

Figure S10. XRD Rietveld analysis of Fe/Ir=3 catalysis revealed that the lattice parameter of the solid solution alloy was determined to be *a*=*b*=*c*=3.7474(8) Å. Comparatively, the lattice parameters of pure Fe and Ir are 3.66 Å and 3.85 Å, respectively. The carbon substrate peaks were excluded in refinement calculation.

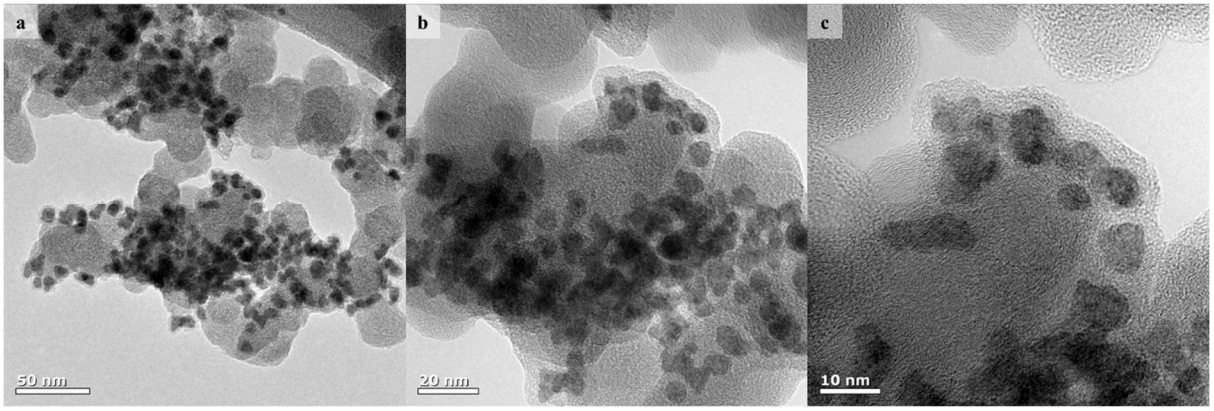

Figure S11. High-resolution transmission electron microscopy (HR-TEM) images of IrFe/C nanoparticles showing well-dispersed 5–10 nm Ir–Fe clusters supported on carbon at (a) x100,000, **(b)** x200,000, and **(c)** x400,000.

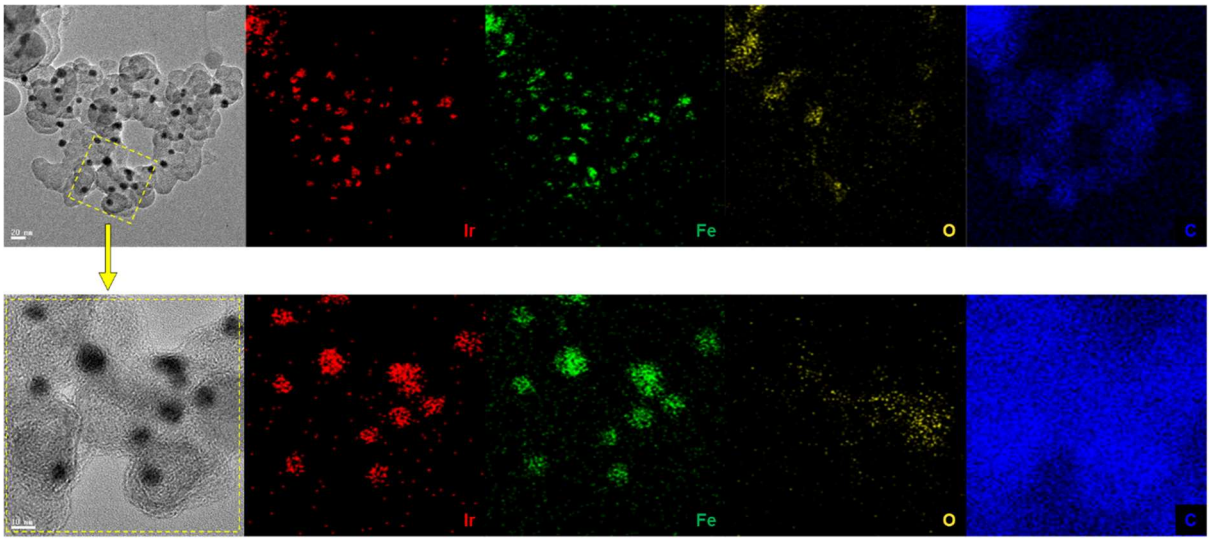

Figure S12. HR-TEM images and corresponding energy-dispersive X-ray spectroscopy (EDS) elemental mapping of IrFe/C, showing co-localization of Ir and Fe, indicating homogeneous alloy distribution at the nanoscale; Ir (red), Fe (green), O (yellow), and C (blue).

Evaluation of Electrochemical Performance and Durability

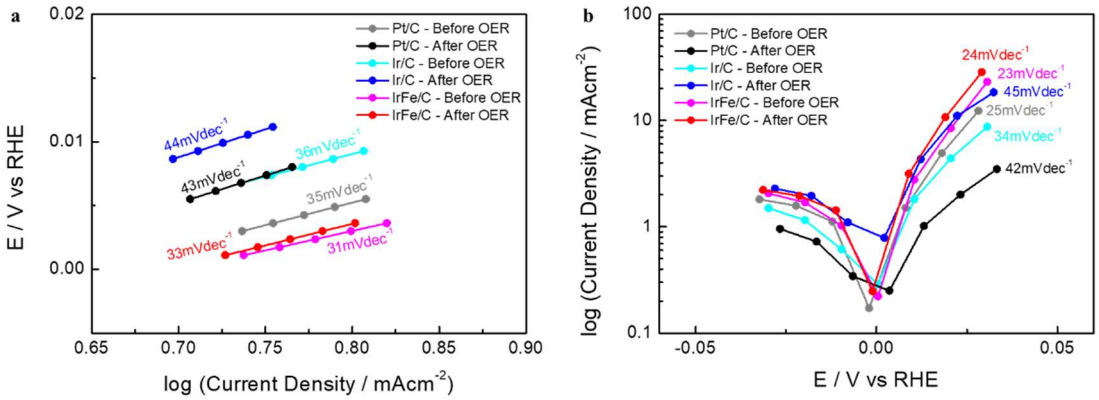

Figure S13. Tafel plot of HER and HOR kinetics for Pt/C, Ir/C, and IrFe/C catalysts before and after OER operation. (a) HER Tafel plots and **(b)** HOR Tafel plots.

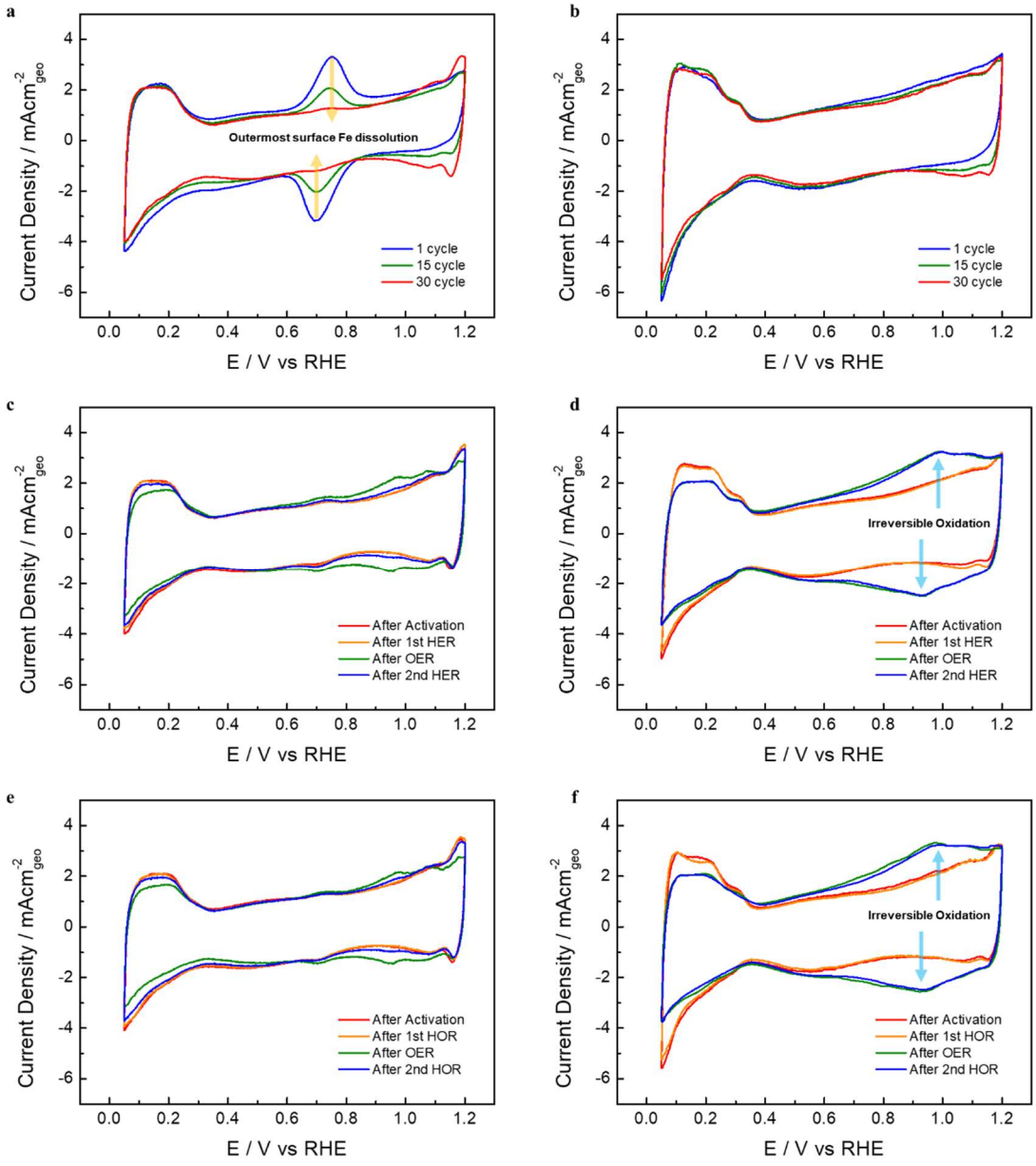

Figure S14. Evolution of cyclic voltammograms (CVs) for (a)(c)(e) IrFe/C and (b)(d)(f) Ir/C catalysts under various electrochemical tests. (a)(b) Activation process, **(c)(d)** Activation → HER → OER → HER process, and **(e)(f)** Activation → HOR → OER → HOR process.

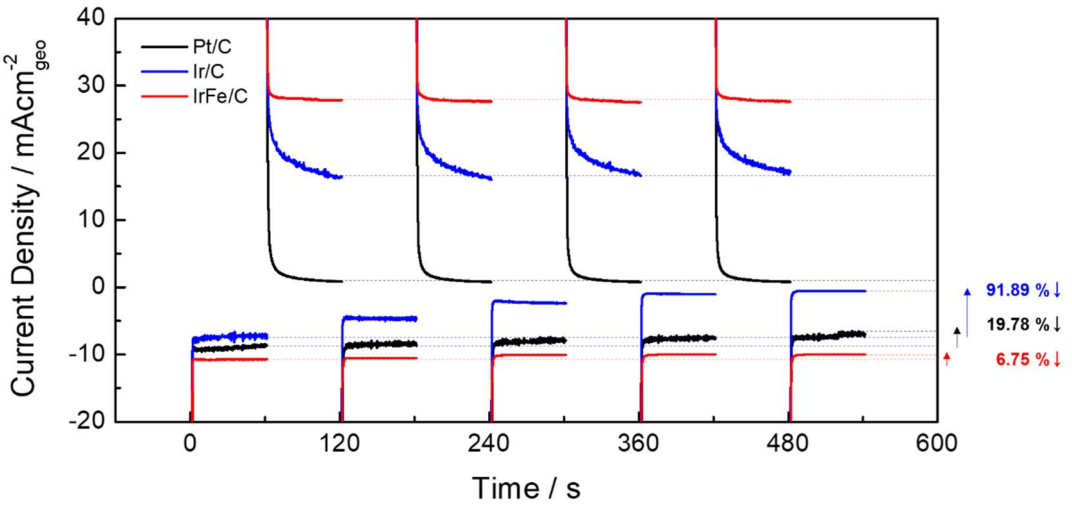

Figure S15. Evaluation of dynamic surface reversibility and regeneration rates via chronoamperometry (CA) profiles. The profiles were recorded for Pt/C, Ir/C, and IrFe/C catalysts while alternating the applied potential between HER (@ –0.1 V) and OER (@ 1.6 V) regions every 60 seconds.

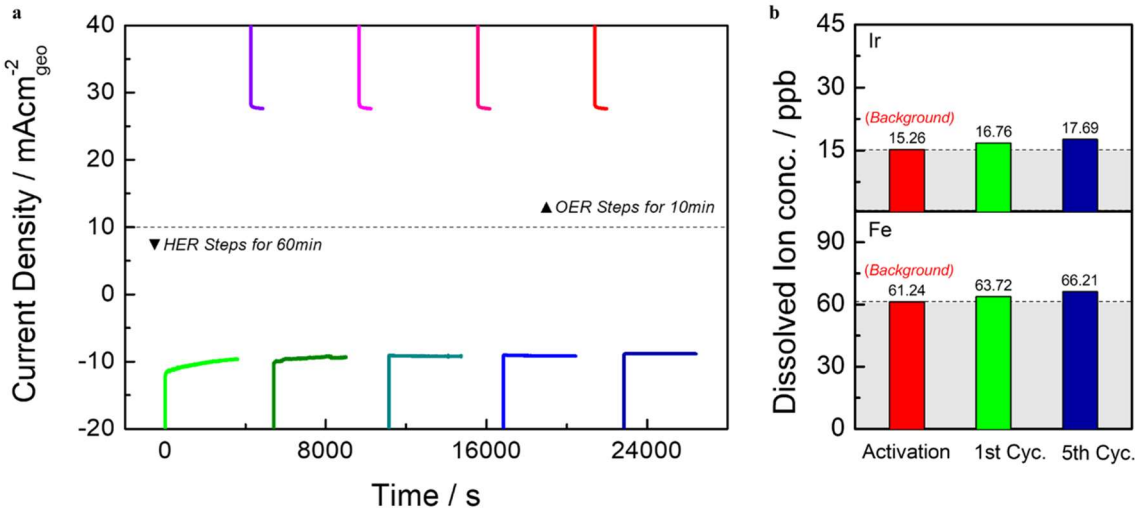

Figure S16. Evaluation of long-term stability under periodic HER-OER potential switching conditions. (a) Chronoamperometric (CA) response of the IrFe/C catalyst recorded by alternating the applied potential between the HER (0.1 V for 60 min) and OER (1.6 V for 10 min) regions. **(b)** Dissolved Ir and Fe ion concentration from IrFe/C catalyst before and after the long-term stability test.

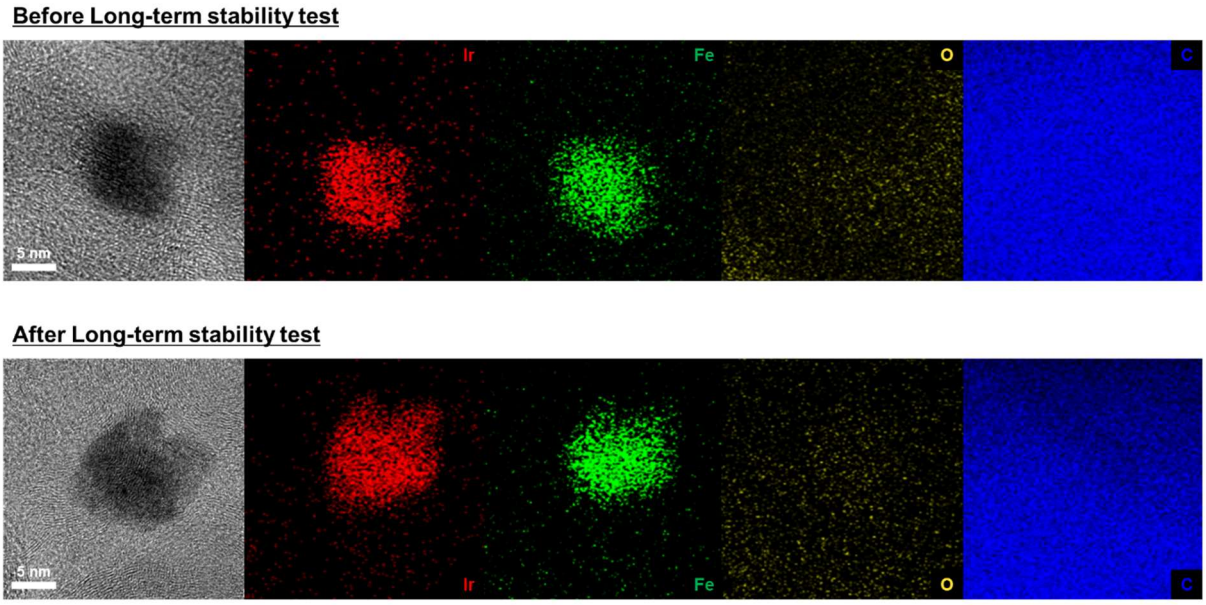

Figure S17. HR-TEM images and corresponding EDS elemental mapping of a single IrFe/C nanoparticle before and after the long-term stability test; Ir (red), Fe (green), O (yellow), and C (blue).

Surface Chemical State Analysis via X-ray Photoelectron Spectroscopy (XPS)

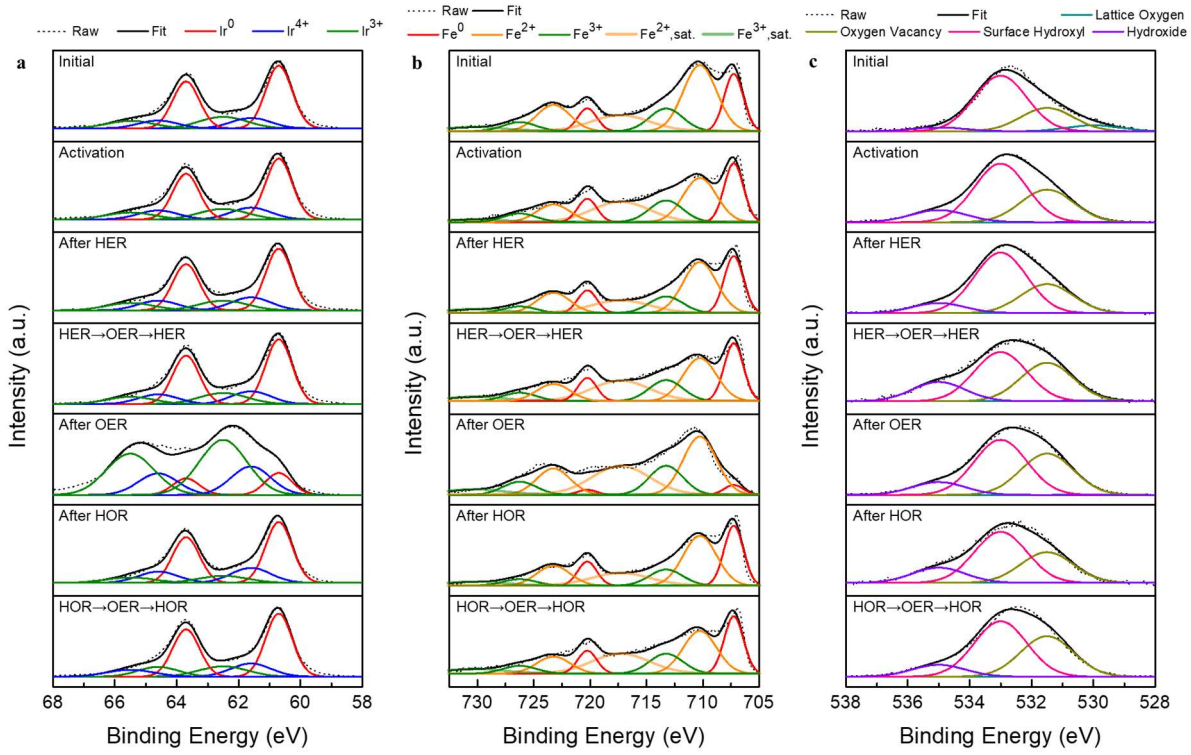

Figure S18. Ex-situ XPS analysis tracking the surface chemical state evolution of the IrFe/C catalyst under various electrochemical stages. High-resolution spectra of (a) Ir *4f*, **(b)** Fe *2p*, and **(c)** O *1s* regions were collected at distinct operational stages: Initial (as-prepared), after Activation, after HER, during the HER→OER→HER sequence, after OER, and during the HOR→OER→HOR sequence.

	Label	Ir^0 $4f_{7/2}$	Ir^0 $4f_{5/2}$	Ir^{4+} $4f_{7/2}$	Ir^{4+} $4f_{5/2}$	Ir^{3+} $4f_{7/2}$	Ir^{3+} $4f_{5/2}$
Initial	Binding Energy (eV)	60.7	63.7	61.6	64.6	62.5	65.5
	FWHM	1	1	1.5	1.5	1.8	1.8
	Height	29155.7	21866.8	4830.15	3622.61	5378.36	3495.93
	Area	31035.4	23276.6	7712.33	5784.25	10305.2	6698.38
	Relative intensity (%)	36.59%	27.44%	9.09%	6.82%	12.15%	7.90
Activation	Binding Energy (eV)	60.7	63.7	61.6	64.6	62.5	65.5
	FWHM	1	1	1.5	1.5	1.8	1.8
	Height	30580.8	22935.6	5905.73	4429.3	5248.64	3411.62
	Area	32552.4	24414.3	9429.72	7072.29	10056.7	6536.82
	Relative intensity (%)	36.14%	27.11%	10.47%	7.85%	11.17%	7.26%
After HER	Binding Energy (eV)	60.7	63.7	61.6	64.6	62.5	65.5
	FWHM	1	1	1.5	1.5	1.8	1.8
	Height	18382.9	13787.1	3814.6	2860.95	2860.5	2145.38
	Area	19567.9	14676	6090.77	4568.08	5480.83	4110.63
	Relative intensity (%)	35.90%	26.90%	11.20%	8.40%	10.10%	7.50%
HER ↓ OER ↓ HER	Binding Energy (eV)	60.7	63.7	61.6	64.6	62.5	65.5
	FWHM	1	1	1.5	1.5	1.8	1.8
	Height	32312.4	24234.3	6341.25	4755.93	5489.11	3567.92
	Area	34395.7	25796.8	10125.1	7593.84	10517.4	6836.31
	Relative intensity (%)	36.11%	27.08%	10.63%	7.97%	11.04%	7.18%
After OER	Binding Energy (eV)	60.7	63.7	61.6	64.6	62.5	65.5
	FWHM	1	1	1.5	1.5	1.8	1.8
	Height	4772.63	3579.47	6207.03	4655.27	11994.1	8995.56
	Area	5080.31	3810.23	9910.76	7433.07	22981.1	17235.9
	Relative intensity (%)	7.60%	5.70%	14.90%	11.20%	34.60%	25.90%
After HOR	Binding Energy (eV)	60.7	63.7	61.6	64.6	62.5	65.5
	FWHM	1	1	1.5	1.5	1.8	1.8
	Height	42515.7	31886.8	10325.3	7743.97	4869.35	3652.02
	Area	45256.5	33942.4	16486.4	12364.8	9329.88	6997.41
	Relative intensity (%)	36.40%	27.30%	13.30%	9.90%	7.50%	5.60%
HOR ↓ OER ↓ HOR	Binding Energy (eV)	60.7	63.7	61.6	64.6	62.5	65.5
	FWHM	1	1	1.5	1.5	1.8	1.8
	Height	31476.5	23607.4	6511.1	4883.32	5103.48	3317.26
	Area	33505.9	25129.4	10396.3	7797.24	9778.52	6356.04
	Relative intensity (%)	36.04%	27.03%	11.18%	8.39%	10.52%	6.84%

Table S1. Ir *4f* core level distribution of IrFe/C in the as-prepared state, after Activation, after HER, after HER→OER→HER, after OER, after HOR, and after HOR→OER→HOR.

	Label	Fe^0 $2p_{3/2}$	Fe^0 $2p_{1/2}$	Fe^{2+} $2p_{3/2}$	Fe^{2+} $2p_{1/2}$	Fe^{3+} $2p_{3/2}$	Fe^{3+} $2p_{1/2}$	Fe^{2+} sat.	Fe^{3+} sat.
Initial	Binding Energy (eV)	707.25	720.25	710.25	723.25	713.25	726.25	717.25	730.25
	FWHM	2	2	3.5	3.5	3.5	3.5	6	6
	Height	23873.7	9549.48	27487.7	10995.1	9471.76	3788.7	6544.89	1657.56
	Area	50825.6	20330.2	102409	40963.7	35288.3	14115.3	41800.9	10586.5
	Relative intensity (%)	16.10%	6.40%	32.40%	13.00%	11.20%	4.50%	13.20%	3.30%
Activation	Binding Energy (eV)	707.25	720.25	710.25	723.25	713.25	726.25	717.25	730.25
	FWHM	2	2	3.5	3.5	3.5	3.5	6	6
	Height	11974.4	4789.77	8992.14	3596.85	4412.05	1764.82	4085.26	499.824
	Area	25492.9	10197.2	33501.6	13400.6	16437.8	6575.11	26091.8	3192.29
	Relative intensity (%)	18.90%	7.56%	24.84%	9.93%	12.19%	4.87%	19.34%	2.37%
After HER	Binding Energy (eV)	707.25	720.25	710.25	723.25	713.25	726.25	717.25	730.25
	FWHM	2	2	3.5	3.5	3.5	3.5	6	6
	Height	33970.7	13588.3	30377.8	12151.1	9896.3	3958.52	7397.12	2219.14
	Area	72321.4	28928.5	113177	45270.6	36870	14748	47244	14173.2
	Relative intensity (%)	19.40%	7.80%	30.40%	12.10%	9.90%	4.00%	12.70%	3.80%
HER ↓ OER ↓ HER	Binding Energy (eV)	707.25	720.25	710.25	723.25	713.25	726.25	717.25	730.25
	FWHM	2	2	3.5	3.5	3.5	3.5	6	6
	Height	12498.6	4999.44	9286.58	3714.63	4555	1822	4351.12	861.067
	Area	26608.8	10643.5	34598.6	13839.4	16970.4	6788.14	27789.9	5499.49
	Relative intensity (%)	18.64%	7.46%	24.24%	9.70%	11.89%	4.76%	19.47%	3.85%
After OER	Binding Energy (eV)	707.25	720.25	710.25	723.25	713.25	726.25	717.25	730.25
	FWHM	2	2	3.5	3.5	3.5	3.5	6	6
	Height	3000	1500	17887.4	8049.33	8896.06	4003.23	8739.72	1556.81
	Area	6386.8	3193.4	66641.9	29988.9	33143.5	14914.6	55818.9	9943.04
	Relative intensity (%)	2.90%	1.50%	30.30%	13.60%	15.10%	6.80%	25.40%	4.50%
After HOR	Binding Energy (eV)	707.25	720.25	710.25	723.25	713.25	726.25	717.25	730.25
	FWHM	2	2	3.5	3.5	3.5	3.5	6	6
	Height	38689.1	15475.7	32109.4	12843.8	10336.3	4134.54	7922.81	2376.84
	Area	82366.6	32946.6	119628	47851.2	38509.4	15403.8	50601.4	15180.4
	Relative intensity (%)	20.50%	8.20%	29.70%	11.90%	9.60%	3.80%	12.60%	3.80%
HOR ↓ OER ↓ HOR	Binding Energy (eV)	707.25	720.25	710.25	723.25	713.25	726.25	717.25	730.25
	FWHM	2	2	3.5	3.5	3.5	3.5	6	6
	Height	12597.4	5038.96	9409.27	3763.71	4382.81	1753.12	4326.02	997.761
	Area	26819.2	10727.7	35055.7	14022.3	16328.8	6531.53	27629.6	6372.53
	Relative intensity (%)	18.69%	7.48%	24.43%	9.77%	11.38%	4.55%	19.26%	4.44%

Table S2. Fe *2p* core level distribution of IrFe/C in the as-prepared state, after Activation, after HER, after HER→OER→HER, after OER, after HOR, and after HOR→OER→HOR.

	Label	Lattice Oxygen	Oxygen Vacancy	Surface Hydroxyl	Hydroxide
Initial	Binding Energy (eV)	530	531.5	533	535
	FWHM	2	2	2	2
	Height	1589.02	6142.79	14603.6	1002.46
	Area	3382.93	13077.6	31090.3	2134.19
	Relative intensity (%)	6.81%	26.32%	62.57%	4.30%
Activation	Binding Energy (eV)	530	531.5	533	535
	FWHM	1.34	2.01	1.98	2.11
	Height	130.012	11675	20941	4317.31
	Area	184.886	24973.9	44056	9695.69
	Relative intensity (%)	0.23%	31.65%	55.83%	12.29%
After HER	Binding Energy (eV)	530	531.5	533	535
	FWHM	2	2	2	2
	Height	10	10188.6	21336.8	3517.87
	Area	21.2894	21691	45424.9	7489.35
	Relative intensity (%)	0.03%	29.07%	60.87%	10.036%
HER ↓ OER ↓ HER	Binding Energy (eV)	530	531.5	533	535
	FWHM	2	2	2	2
	Height	58.8121	2216.17	2839.06	1112.82
	Area	125.208	4718.1	6044.2	2369.13
	Relative intensity (%)	0.94%	35.59%	45.59%	17.87%
After OER	Binding Energy (eV)	530	531.5	533	535
	FWHM	2	2	2	2
	Height	40.925	15921.3	21278.1	4920.77
	Area	87.127	33895.5	45299.9	10476.1
	Relative intensity (%)	0.10%	37.76%	50.47%	11.67%
After HOR	Binding Energy (eV)	530	531.5	533	535
	FWHM	2	2	2	2
	Height	10	1885.23	3142.42	937.801
	Area	21.2894	4013.56	6690.04	1996.53
	Relative intensity (%)	0.17%	31.55%	52.59%	15.69%
HOR ↓ OER ↓ HOR	Binding Energy (eV)	530	531.5	533	535
	FWHM	2	2	2	2
	Height	10	17248.9	23596.8	5015.38
	Area	21.2894	36722	50236.2	10677.5
	Relative intensity (%)	0.02%	37.60%	51.44%	10.93%

Table S3. O *1s* core level distribution of IrFe/C in the as-prepared state, after Activation, after HER, after HER→OER→HER, after OER, after HOR, and after HOR→OER→HOR.

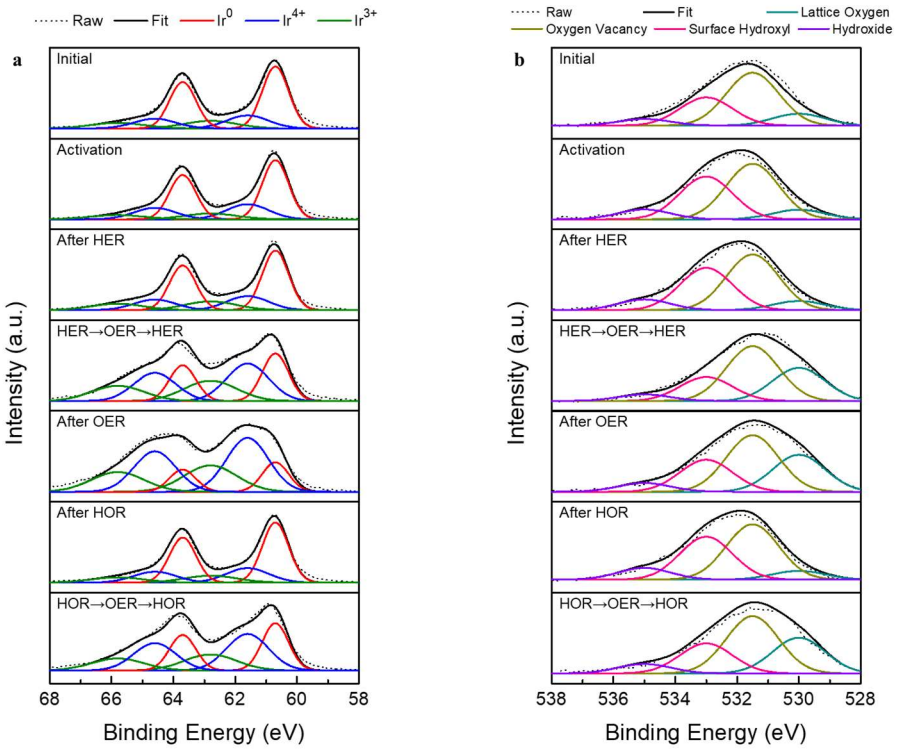

Figure S19. Ex-situ XPS analysis tracking the surface chemical state evolution of the Ir/C catalyst under various electrochemical stages. High-resolution spectra of (a) Ir *4f* and **(b)** O *1s* regions were collected at distinct operational stages: Initial (as-prepared), after Activation, after HER, during the HER→OER→HER sequence, after OER, and during the HOR→OER→HOR sequence.

	Label	Ir^0 $4f_{7/2}$	Ir^0 $4f_{5/2}$	Ir^{4+} $4f_{7/2}$	Ir^{4+} $4f_{5/2}$	Ir^{3+} $4f_{7/2}$	Ir^{3+} $4f_{5/2}$
Initial	Binding Energy (eV)	60.7	63.7	61.6	64.6	62.8	65.8
	FWHM	1	1	1.6	1.6	2	2
	Height	126789	95091.9	26533.3	19900	15502	11626.5
	Area	134964	101223	45190.4	33892.8	33002.9	24752.2
	Relative intensity (%)	36.18%	27.14%	12.11%	9.09%	8.85%	6.64%
Activation	Binding Energy (eV)	60.7	63.7	61.6	64.6	62.8	65.8
	FWHM	1	1	1.6	1.6	2	2
	Height	147734	110800	37665.2	28248.9	14509.8	10882.4
	Area	157259	117944	64149.7	48112.3	30890.6	23167.9
	Relative intensity (%)	35.62%	26.71%	14.53%	10.90%	7.00%	5.25%
After HER	Binding Energy (eV)	60.7	63.7	61.6	64.6	62.8	65.8
	FWHM	1	1	1.6	1.6	2	2
	Height	86333.2	64749.9	20234.2	15175.7	12405	9303.74
	Area	91899.2	68924.4	34462	25846.5	26409.5	19807.1
	Relative intensity (%)	34.37%	25.78%	12.89%	9.67%	9.88%	7.41%
HER ↓ OER ↓ HER	Binding Energy (eV)	60.7	63.7	61.6	64.6	62.8	65.8
	FWHM	1	1	1.6	1.6	2	2
	Height	6135.24	4601.43	4827.53	3620.65	2609.82	1957.36
	Area	6530.79	4898.09	8222.03	6166.53	5556.16	4167.12
	Relative intensity (%)	18.38%	13.78%	23.13%	17.35%	15.63%	11.72%
After OER	Binding Energy (eV)	60.7	63.7	61.6	64.6	62.8	65.8
	FWHM	1	1	1.6	1.6	2	2
	Height	3204.54	2403.41	5862.85	4397.14	2853.89	2140.42
	Area	3411.15	2558.36	9985.34	7489.01	6075.77	4556.83
	Relative intensity (%)	10.01%	7.51%	29.30%	21.98%	17.83%	13.37%
After HOR	Binding Energy (eV)	60.7	63.7	61.6	64.6	62.8	65.8
	FWHM	1	1	1.6	1.6	2	2
	Height	119759	89819.4	28579.8	21434.8	13454.5	10090.9
	Area	127480	95610.3	48675.8	36506.8	28643.9	21482.9
	Relative intensity (%)	35.57%	26.68%	13.58%	10.19%	7.99%	5.99%
HOR ↓ OER ↓ HOR	Binding Energy (eV)	60.7	63.7	61.6	64.6	62.8	65.8
	FWHM	1	1	1.6	1.6	2	2
	Height	7111.06	5333.3	5487.43	4115.57	2399.51	1799.63
	Area	7569.53	5677.15	9345.94	7009.46	5108.43	3831.32
	Relative intensity (%)	19.64%	14.73%	24.25%	18.19%	13.25%	9.94%

Table S4. Ir *4f* core level distribution of Ir/C in the as-prepared state, after Activation, after HER, after HER→OER→HER, after OER, after HOR, and after HOR→OER→HOR.

	Label	Lattice Oxygen	Oxygen Vacancy	Surface Hydroxyl	Hydroxide
Initial	Binding Energy (eV)	530	531.5	533	535
	FWHM	2	2	2	2
	Height	3262.62	14495.9	7701.29	1817.27
	Area	6945.94	30860.9	16395.6	3868.87
	Relative intensity (%)	11.96%	53.14%	28.23%	6.66%
Activation	Binding Energy (eV)	530	531.5	533	535
	FWHM	2	2	2	2
	Height	2098.95	12131.7	9371.06	2150.64
	Area	4468.54	25827.7	19950.5	4578.58
	Relative intensity (%)	8.15%	47.11%	36.39%	8.35%
After HER	Binding Energy (eV)	530	531.5	533	535
	FWHM	2	2	2	2
	Height	2061.1	12715.1	9663.58	2430.24
	Area	4387.96	27069.7	20573.2	5173.85
	Relative intensity (%)	7.67%	47.32%	35.96%	9.04%
HER ↓ OER ↓ HER	Binding Energy (eV)	530	531.5	533	535
	FWHM	2	2	2	2
	Height	9880.13	16318.4	7146.04	1958.97
	Area	21034.2	34741	15213.5	4170.54
	Relative intensity (%)	27.99%	46.22%	20.24%	5.55%
After OER	Binding Energy (eV)	530	531.5	533	535
	FWHM	2	2	2	2
	Height	8411.4	12886.8	7290.04	1951.45
	Area	17907.4	27435.2	15520.1	4154.53
	Relative intensity (%)	27.54%	42.20%	23.87%	6.39%
After HOR	Binding Energy (eV)	530	531.5	533	535
	FWHM	2	2	2	2
	Height	1964.99	12386.1	9605.2	2620.87
	Area	4183.36	26369.3	20448.9	5579.69
	Relative intensity (%)	7.39%	46.60%	36.14%	9.86%
HOR ↓ OER ↓ HOR	Binding Energy (eV)	530	531.5	533	535
	FWHM	2	2	2	2
	Height	7781.01	12482.8	6533.02	2048.41
	Area	16565.3	26575.2	13908.4	4360.96
	Relative intensity (%)	26.97%	43.28%	22.65%	7.10%

Table S5. O *1s* core level distribution of Ir/C in the as-prepared state, after Activation, after HER, after HER→OER→HER, after OER, after HOR, and after HOR→OER→HOR.

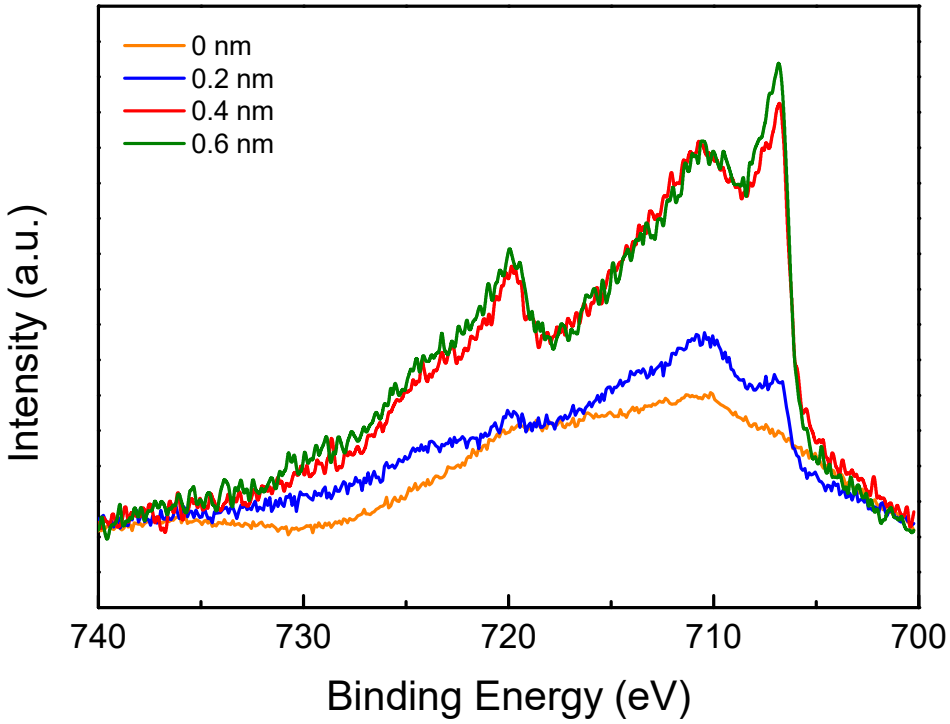

Figure S20. XPS depth profile analysis of the Fe 2p region for the activated IrFe/C catalyst. The spectra were collected at controlled etching depths (0, 0.2, 0.4, and 0.6 nm) using Ar ion sputtering.

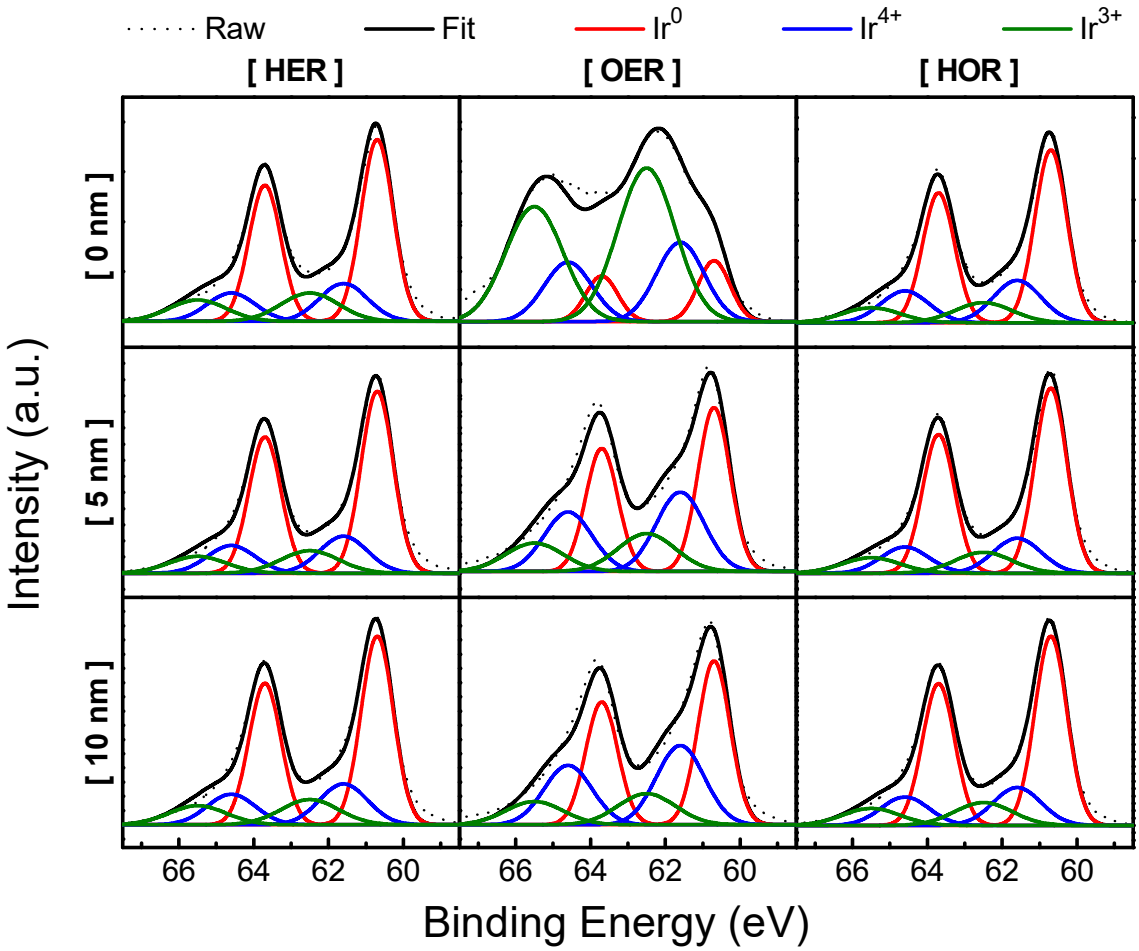

Figure S21. XPS spectra of Ir 4f IrFe/C after HER, OER, and after HOR at 0, 5, and 10 nm depth.

	Label	Ir^0 $4f_{7/2}$	Ir^0 $4f_{5/2}$	Ir^{4+} $4f_{7/2}$	Ir^{4+} $4f_{5/2}$	Ir^{3+} $4f_{7/2}$	Ir^{3+} $4f_{5/2}$
After HER	Binding Energy (eV)	60.7	63.7	61.6	64.6	62.5	65.5
	FWHM	1	1	1.5	1.5	1.8	1.8
	Height	56797	42597.8	11479.3	8609.51	6985	5238.75
	Area	60458.5	45343.9	18329.1	13746.8	13383.5	10037.7
	Relative intensity (%)	37.50%	28.10%	11.40%	8.50%	8.30%	6.20%
After OER	Binding Energy (eV)	60.7	63.7	61.6	64.6	62.5	65.5
	FWHM	1	1	1.5	1.5	1.8	1.8
	Height	47953.8	35965.3	23099.4	17324.6	11031	8273.24
	Area	51045.2	38283.9	36882.8	27662.1	21135.8	15851.9
	Relative intensity (%)	26.70%	20.10%	19.30%	14.50%	11.10%	8.30%
After HOR	Binding Energy (eV)	60.7	63.7	61.6	64.6	62.5	65.5
	FWHM	1	1	1.5	1.5	1.8	1.8
	Height	115597	86697.9	21674.1	16255.6	12914.5	9685.91
	Area	123049	92287	34607.1	25955.3	24744.8	18558.6
	Relative intensity (%)	38.50%	28.90%	10.80%	8.10%	7.80%	5.80%

Table S6. Ir 4f core level distribution of IrFe/C after HER, after OER, and after HOR at 5 nm depth.

	Label	Ir^0 $4f_{7/2}$	Ir^0 $4f_{5/2}$	Ir^{4+} $4f_{7/2}$	Ir^{4+} $4f_{5/2}$	Ir^{3+} $4f_{7/2}$	Ir^{3+} $4f_{5/2}$
After HER	Binding Energy (eV)	60.7	63.7	61.6	64.6	62.5	65.5
	FWHM	1	1	1.5	1.5	1.8	1.8
	Height	66948.7	50211.5	14417.5	10813.1	8910.77	6683.08
	Area	71264.6	53448.5	23020.5	17265.4	17073.4	12805
	Relative intensity (%)	36.60%	27.40%	11.80%	8.90%	8.80%	6.60%
After OER	Binding Energy (eV)	60.7	63.7	61.6	64.6	62.5	65.5
	FWHM	1	1	1.5	1.5	1.8	1.8
	Height	58109.2	43581.9	27960.1	20970.1	10937.8	8203.37
	Area	61855.4	46391.5	44643.9	33482.9	20957.3	15718
	Relative intensity (%)	27.70%	20.80%	20.00%	15.00%	9.40%	7.00%
After HOR	Binding Energy (eV)	60.7	63.7	61.6	64.6	62.5	65.5
	FWHM	1	1	1.5	1.5	1.8	1.8
	Height	129615	97211.5	25865.4	19399	15540.2	11655.2
	Area	137971	103478	41299.2	30974.4	29775.7	22331.8
	Relative intensity (%)	37.70%	28.30%	11.30%	8.50%	8.10%	6.10%

Table S7. Ir 4f core level distribution of IrFe/C after HER, after OER, and after HOR at 10 nm depth.

Bulk Local Structural Analysis via X-ray Absorption Spectroscopy (XAS)

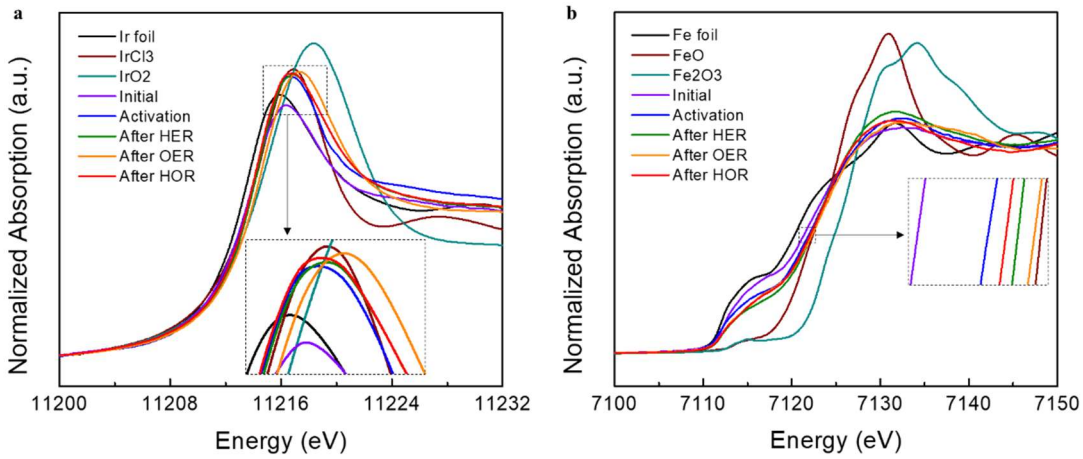

Figure S22. Structural characterization by XAS analysis. Comparison between the experimental XANES spectra of (a) Ir L_3-edge and **(b)** Fe K-edge for IrFe/C in the as-prepared state, after Activation, after HER, after OER, and after HOR. The white-line intensity indicates that the oxidation state of Ir increases in the order of Initial < Ir foil < Activation ≈ HER ≈ HOR < OER < $IrCl_3$ < IrO_2. The absorption edge position suggests that the oxidation state of Fe increases in the order of Fe foil < Initial < Activation < HOR < HER < OER < FeO < Fe_2O_3.

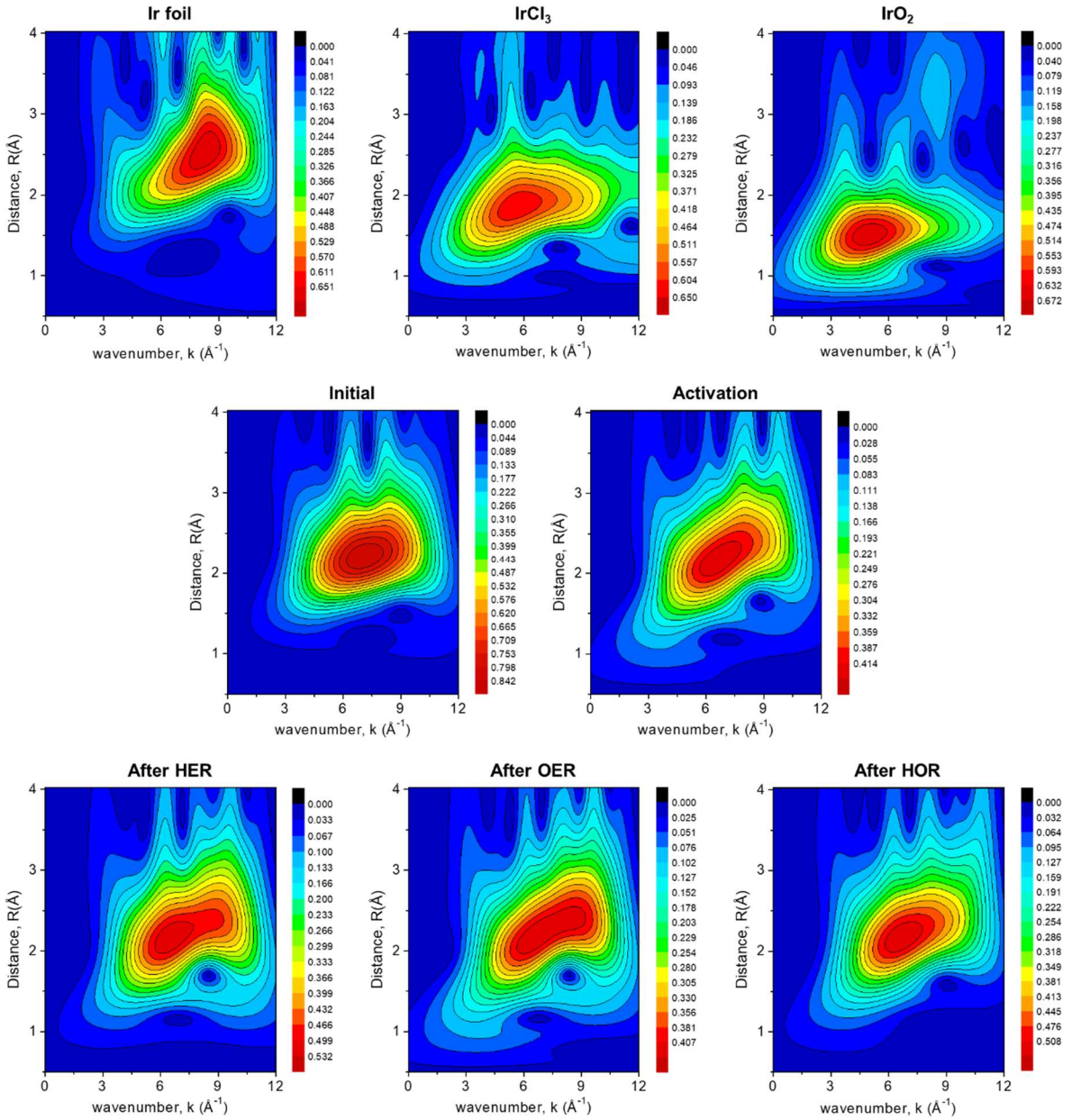

Figure S23. Ir L_3-edge Wavelet-transformed (WT)-EXAFS analyses for Ir foil, $IrCl_3$, IrO_2 and IrFe/C in the as-prepared state, after Activation, after HER, after OER, and after HOR.

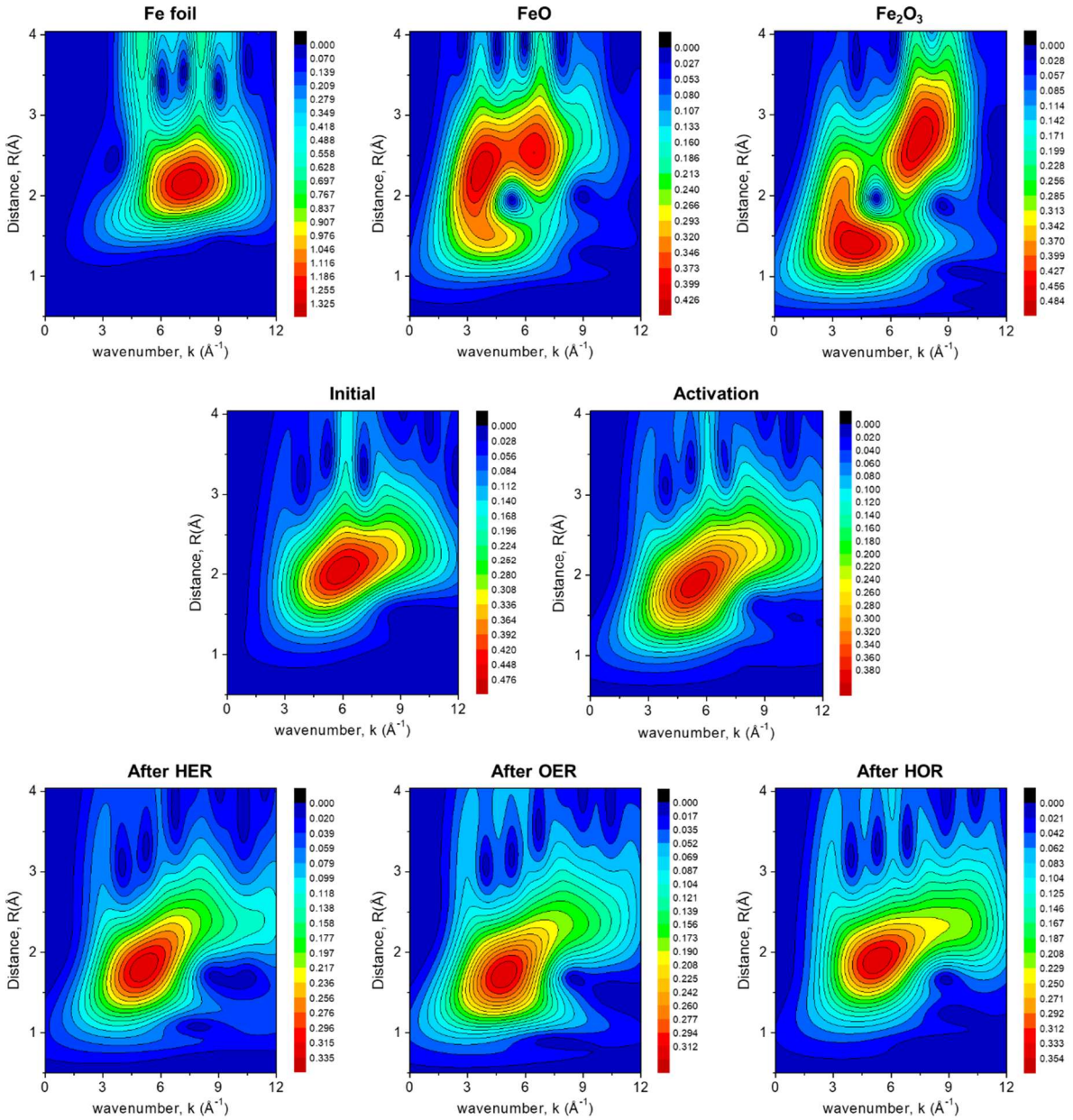

Figure S24. Fe K-edge Wavelet-transformed (WT)-EXAFS analyses for Fe foil, FeO, Fe_2O_3 and IrFe/C in the as-prepared state, after Activation, after HER, after OER, and after HOR.

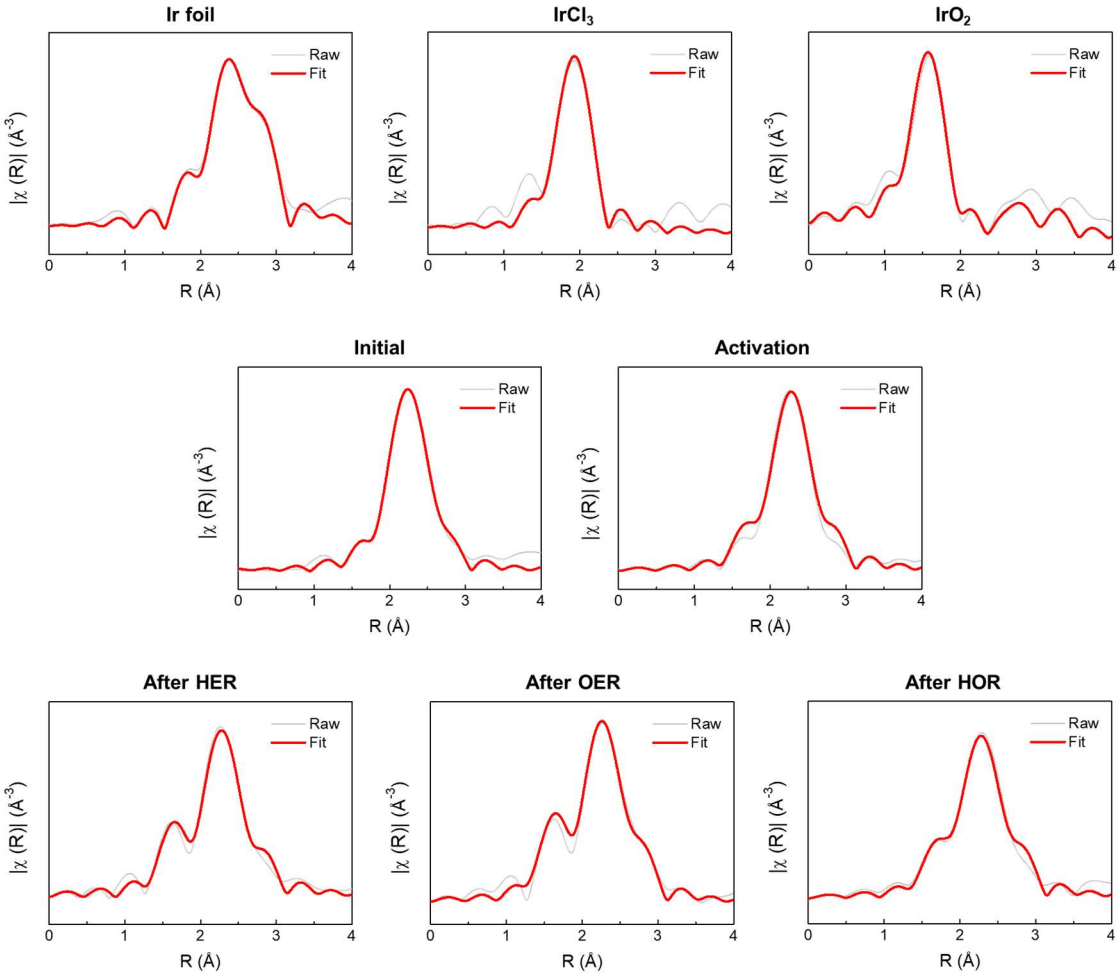

Figure S25. R space and inverse Fourier Transformed (FT) magnitudes of the experimental EXAFS fitting result of Ir L_3-edge for Ir foil, $IrCl_3$, IrO_2 and IrFe/C in the as-prepared state, after Activation, after HER, after OER, and after HOR.

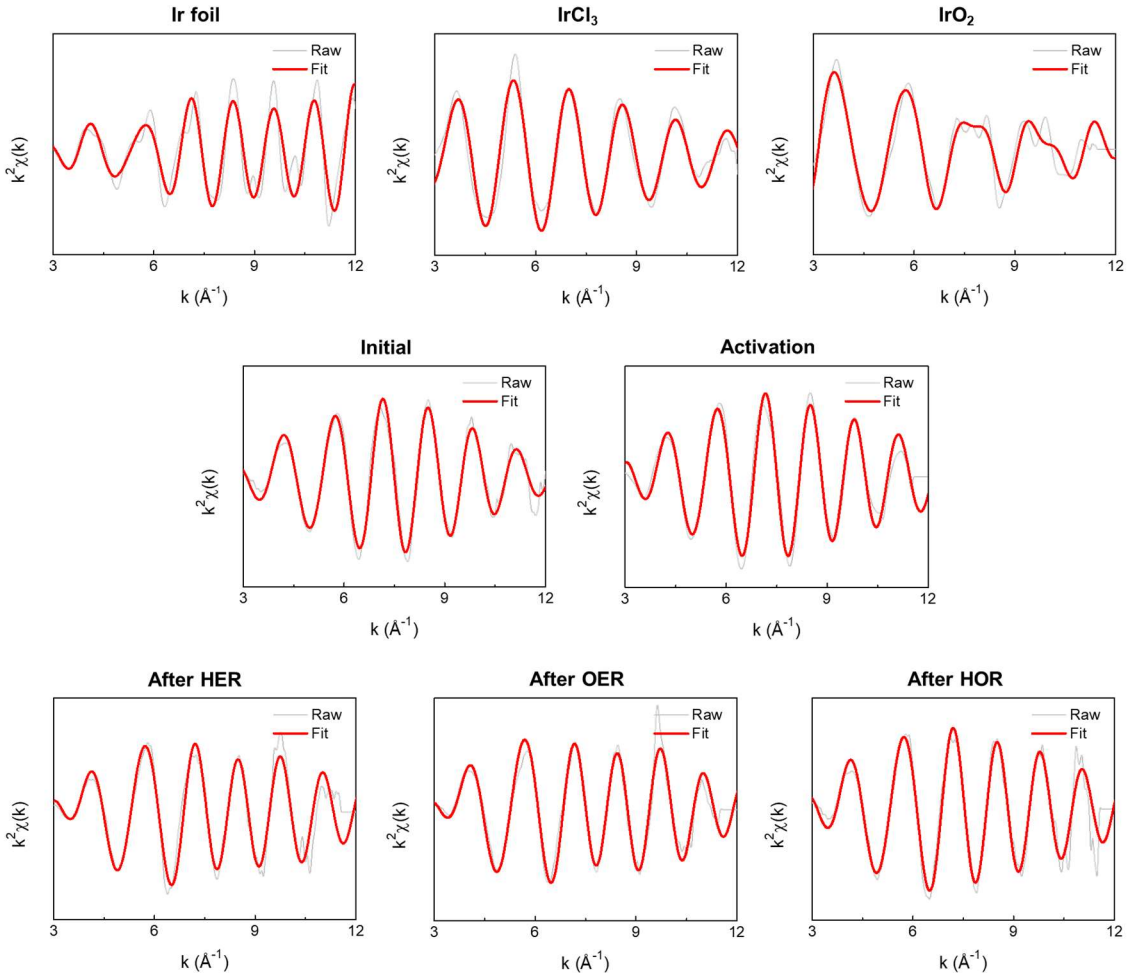

Figure S26. EXAFS spectra in k-space data and corresponding fitting result of Ir L_3-edge for Ir foil, $IrCl_3$, IrO_2 and IrFe/C in the as-prepared state, after Activation, after HER, after OER, and after HOR

Catalysts	Scattering Path	Coordination Number	R(Å)	$\sigma^2(10^{-3}Å^2)$	ΔE_0 (eV)	R-factor
Ir foil	Ir-Ir_1	12*	2.74±0.00	3.06±0.22	6.65±0.71	0.003
	Ir-Ir_2	2*	3.18±0.03	4.26±3.31		
$IrCl_3$	Ir-Cl	6	2.34±0.01	3.40±0.81	7.97±1.90	0.025
IrO_2	Ir-O	6	1.98±0.01	2.69±0.75	9.75±0.02	0.020
	Ir-Ir	4	3.13±0.02	5.10±2.86		
Initial	Ir-Fe	4	2.59±0.01	3.56±0.64	6.58±1.20	0.012
	Ir-Ir	8	2.67±0.02	8.00±1.49		
Activation	Ir-O	1	2.04±0.06	3.06±2.28	9.28±1.36	0.025
	Ir-Fe	3	2.62±0.02	3.25±0.88		
	Ir-Ir	8	2.66±0.02	9.87±1.84		
After HER	Ir-O	1	1.98±0.03	2.64±1.78	7.48±2.58	0.025
	Ir-Fe	3	2.62±0.02	5.78±1.89		
	Ir-Ir	8	2.66±0.03	6.23±2.02		
After OER	Ir-O	1	1.96±0.06	4.07±3.78	4.44±4.20	0.025
	Ir-Fe	3	2.60±0.00	5.71±2.33		
	Ir-Ir	8	2.66±0.04	7.32±2.83		
After HOR	Ir-O	1	1.98±0.03	4.53±4.20	5.91±1.20	0.010
	Ir-Fe	3	2.62±0.01	6.19±0.77		
	Ir-Ir	8	2.66±0.01	6.67±0.85		

Table S8. Structural parameters for Ir foil, $IrCl_3$, IrO_2 and IrFe/C in the as-prepared state, after Activation, after HER, after OER, and after HOR extracted from the EXAFS fitting ($S0^2$=0.78). $S0^2$, amplitude reduction factor (obtained by the fitting of Ir foil); R(Å), interatomic distance (the bond length between Ir central atoms and surrounding coordination atoms); $\sigma^2(10^{-3}Å^2)$, Debye-Waller factor (a measure of thermal and static disorder in absorber-scatterer distances); ΔE_0 (eV), edge-energy shift (the difference between the zero kinetic energy value of the sample and that of the theoretical model); R factor, value the goodness of the fitting. *This value was fixed during EXAFS fitting, based on the known structure of Ir metal.

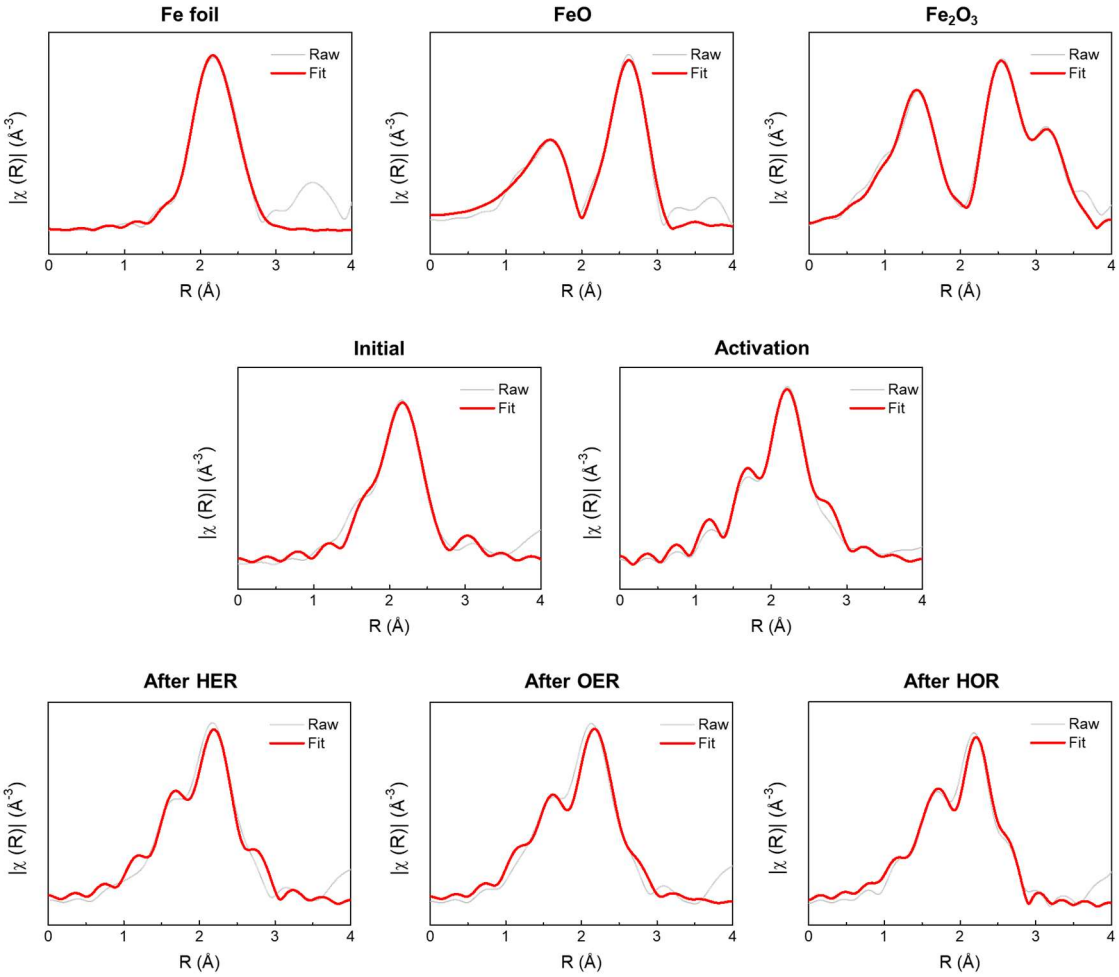

Figure S27. R space and inverse Fourier Transformed (FT) magnitudes of the experimental EXAFS fitting result of Fe K-edge for Fe foil, FeO, FeO_2O_3 and IrFe/C in the as-prepared state, after Activation, after HER, after OER, and after HOR.

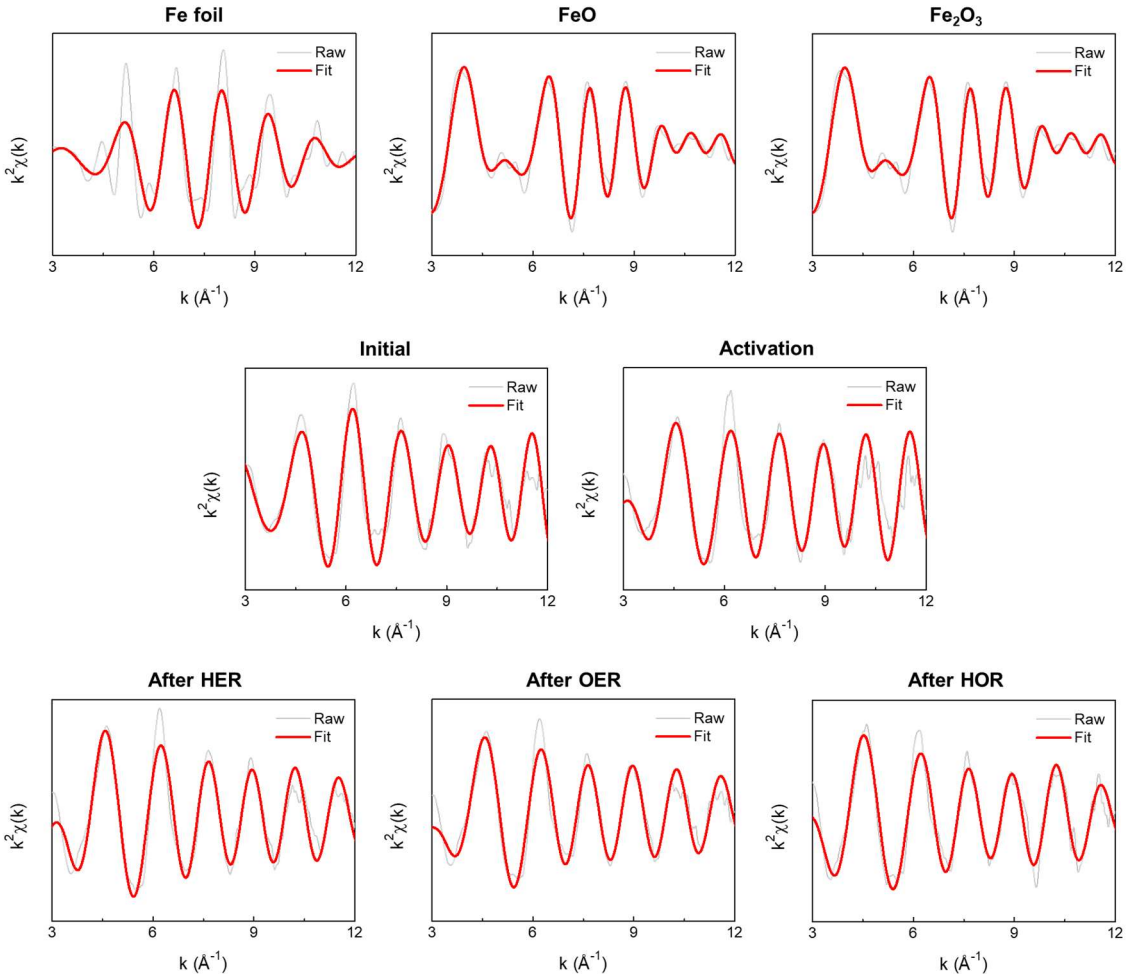

Figure S28. EXAFS spectra in k-space data and corresponding fitting result of Fe K-edge for Fe foil, FeO, FeO_2O_3 and IrFe/C in the as-prepared state, after Activation, after HER, after OER, and after HOR.

Catalysts	Scattering Path	Coordination Number	R(Å)	$\sigma^2(10^{-3}Å^2)$	ΔE_0 (eV)	R-factor
Fe foil	Fe-Fe_1	8	2.46±0.01	5.37±0.87	-2.37±1.40	0.010
	Fe-Fe_2	6	2.84±0.01	5.37±0.87		
FeO	Fe-O_1	6	2.12±0.01	9.06±1.13	-2.01±0.71	0.007
	Fe-Fe_1	12	3.07±0.01	9.52±0.51		
Fe_2O_3	Fe-O_1	3	1.92±0.02	2.91±1.98	-5.49±1.69	0.008
	Fe-O_2	3	2.07±0.03	3.83±3.33		
	Fe-Fe_1	3	2.93±0.01	4.06±0.88		
	Fe-Fe_2	4	3.37±0.02	4.19±1.29		
	Fe-Fe_3	5	3.66±0.02	7.22±2.11		
Initial	Fe-Fe_1	1	2.49±0.03	3.32±2.40	-9.82±1.32	0.012
	Fe-Ir	4	2.59±0.01	3.56±0.64		
	Fe-Fe_2	2	3.06±0.01	5.97±1.59		
Activation	Fe-O_1	1	1.80±0.02	3.07±3.03	-0.51±0.44	0.025
	Fe-O_2	2	2.02±0.04	3.18±2.84		
	Fe-Ir	3	2.62±0.02	3.25±0.88		
	Fe-Fe	2	2.63±0.02	6.17±3.26		
After HER	Fe-O_1	1	1.80±0.01	5.01±1.85	1.24±0.69	0.025
	Fe-O_2	2	2.00±0.02	5.27±1.67		
	Fe-Ir	3	2.62±0.02	5.78±1.89		
	Fe-Fe	2	2.63±0.01	8.76±2.79		
After OER	Fe-O_1	1	1.80±0.04	1.40±1.36	-0.46±0.38	0.025
	Fe-O_2	2	1.99±0.02	4.75±3.23		
	Fe-Ir	3	2.60±0.00	5.71±2.33		
	Fe-Fe	2	2.61±0.01	5.92±1.43		
After HOR	Fe-O_1	1	1.79±0.04	2.69±2.59	-2.92±1.03	0.010
	Fe-O_2	2	1.96±0.02	3.08±1.49		
	Fe-Ir	3	2.62±0.02	6.19±0.77		
	Fe-Fe	2	2.63±0.01	8.02±1.27		

Table S9. Structural parameters for Fe foil, FeO, FeO_2O_3 and IrFe/C in the as-prepared state, after Activation, after HER, after OER, and after HOR extracted from the EXAFS fitting ($S0^2$=0.77). $S0^2$, amplitude reduction factor (obtained by the fitting of Fe foil); R(Å), interatomic distance (the bond length between Fe central atoms and surrounding coordination atoms); $\sigma^2(10^{-3}Å^2)$, Debye-Waller factor (a measure of thermal and static disorder in absorber-scatterer distances); ΔE_0 (eV), edge-energy shift (the difference between the zero kinetic energy value of the sample and that of the theoretical model); R factor, value the goodness of the fitting. *This value was fixed during EXAFS fitting, based on the known structure of Fe metal.

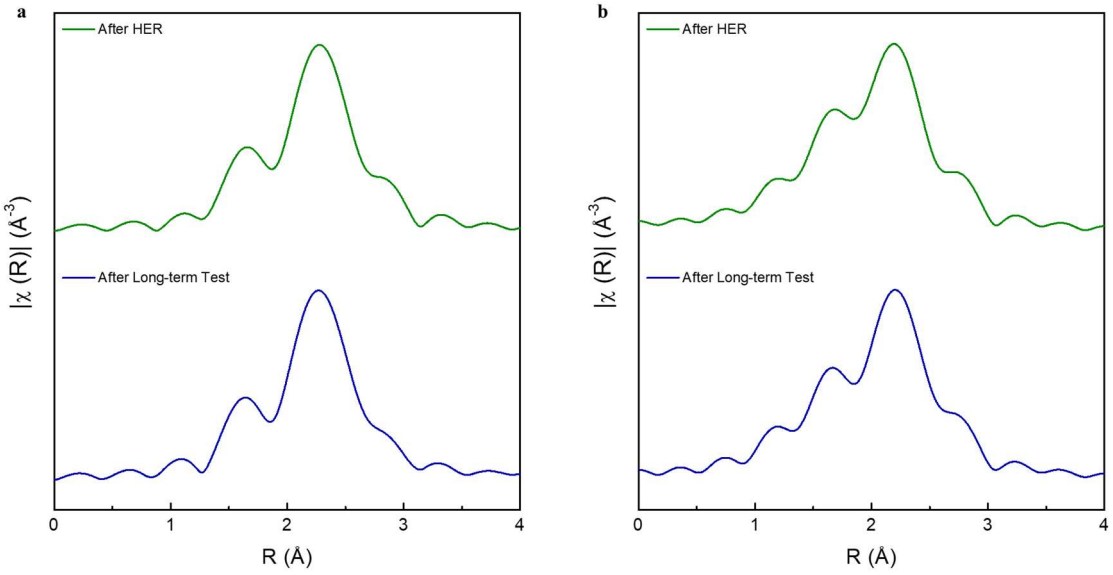

Figure S29. Comparison the FT-EXAFS spectra at the (a) Ir L_3-edge and **(b)** Fe K-edge for the IrFe/C catalyst after the HER process and after the long-term stability test.

Catalysts	Scattering Path	Coordination Number	R(Å)	$\sigma^2(10^{-3}Å^2)$	ΔE_0 (eV)	R-factor
After HER	Ir-O	1	1.98±0.03	2.64±1.78	7.48±2.58	0.025
	Ir-Fe	3	2.62±0.02	5.78±1.89		
	Ir-Ir	8	2.66±0.03	6.23±2.02		
	$Fe-O_1$	1	1.80±0.01	5.01±1.85	1.24±0.69	
	$Fe-O_2$	2	2.00±0.02	5.27±1.67		
	Fe-Ir	3	2.62±0.02	5.78±1.89		
	Fe-Fe	2	2.63±0.01	8.76±2.79		
After Long-term Test	Ir-O	1	1.98±0.04	4.16±3.95	6.81±2.61	0.024
	Ir-Fe	3	2.62±0.02	5.13±1.88		
	Ir-Ir	8	2.65±0.03	7.59±2.74		
	$Fe-O_1$	1	1.80±0.00	3.04±2.49	1.13±0.77	
	$Fe-O_2$	2	2.00±0.02	4.24±3.74		
	Fe-Ir	3	2.62±0.02	5.13±1.88		
	Fe-Fe	2	2.63±0.01	5.98±2.51		

Table S10. Structural parameters derived from the EXAFS fitting at the Ir L_3-edge and Fe K-edge for the IrFe/C catalyst after HER and after the long-term stability test.

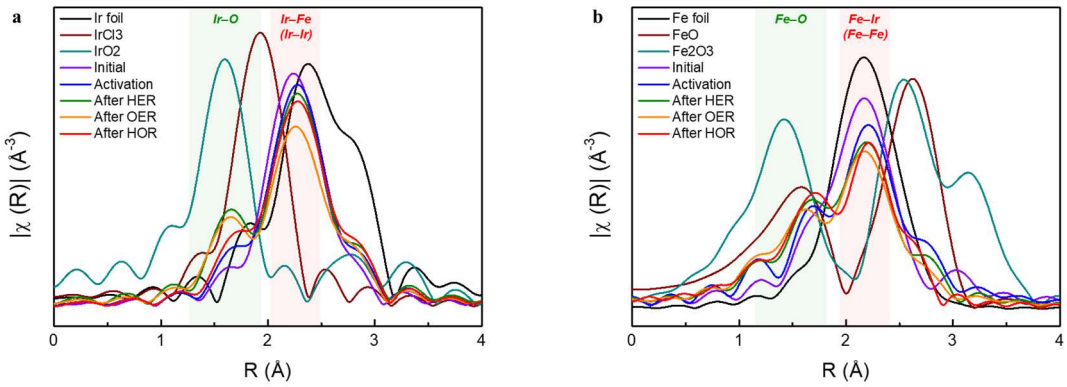

Figure S30. Structural characterization by XAS analysis of peak intensity. Comparison the FT-EXAFS signals of **(a)** Ir L_3-edge and **(b)** Fe K-edge for IrFe/C in the as-prepared state, after Activation, after HER, after OER, and after HOR.

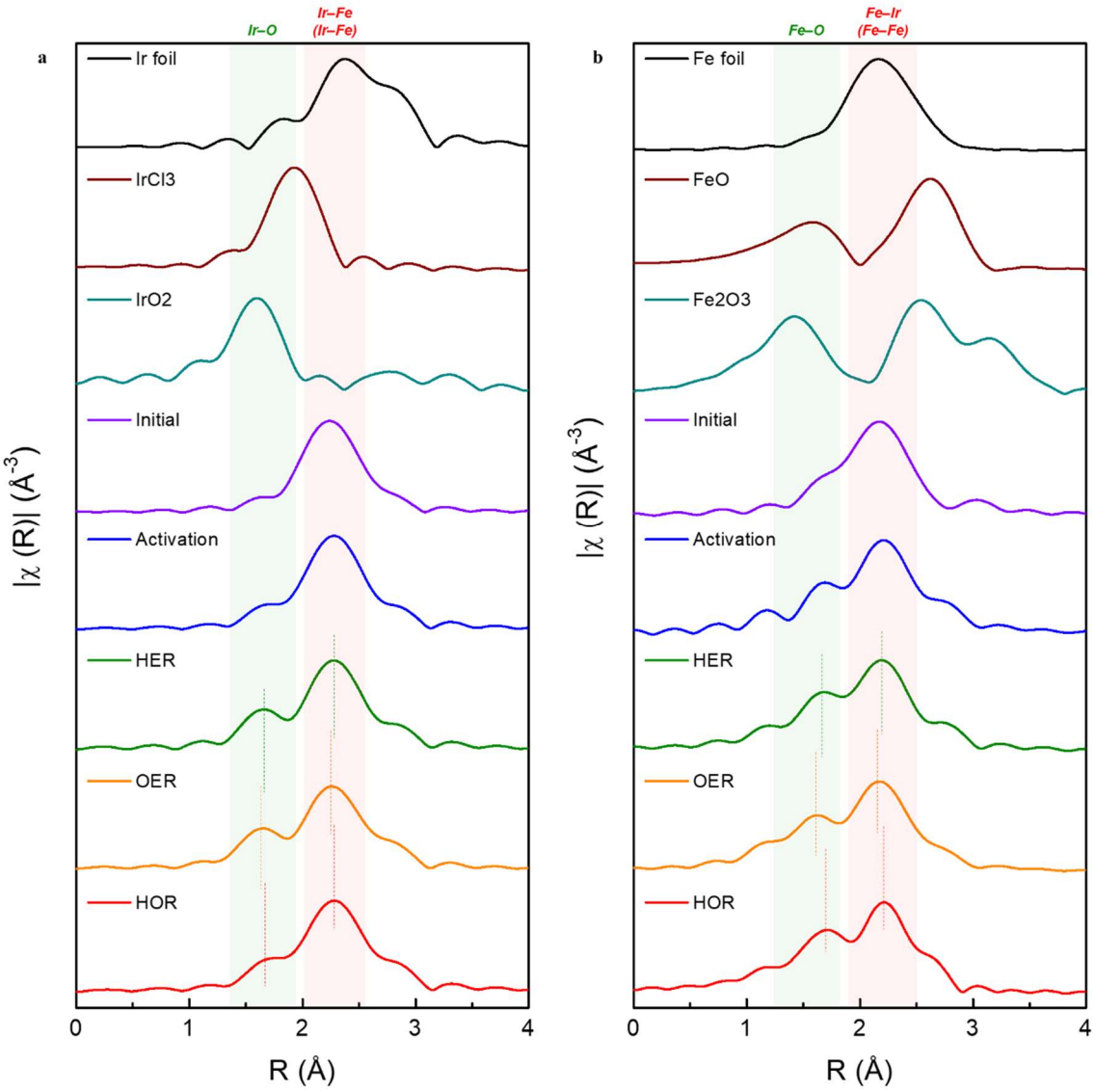

Figure S31. Structural characterization by XAS analysis of interatomic distances. Comparison the k^2-weighted FT-EXAFS spectra of **(a)** Ir L_3-edge and **(b)** Fe K-edge for IrFe/C in the as-prepared state, after Activation, after HER, after OER, and after HOR.

Density Functional Theory (DFT) Calculations for Reaction Energetics and Surface Stability

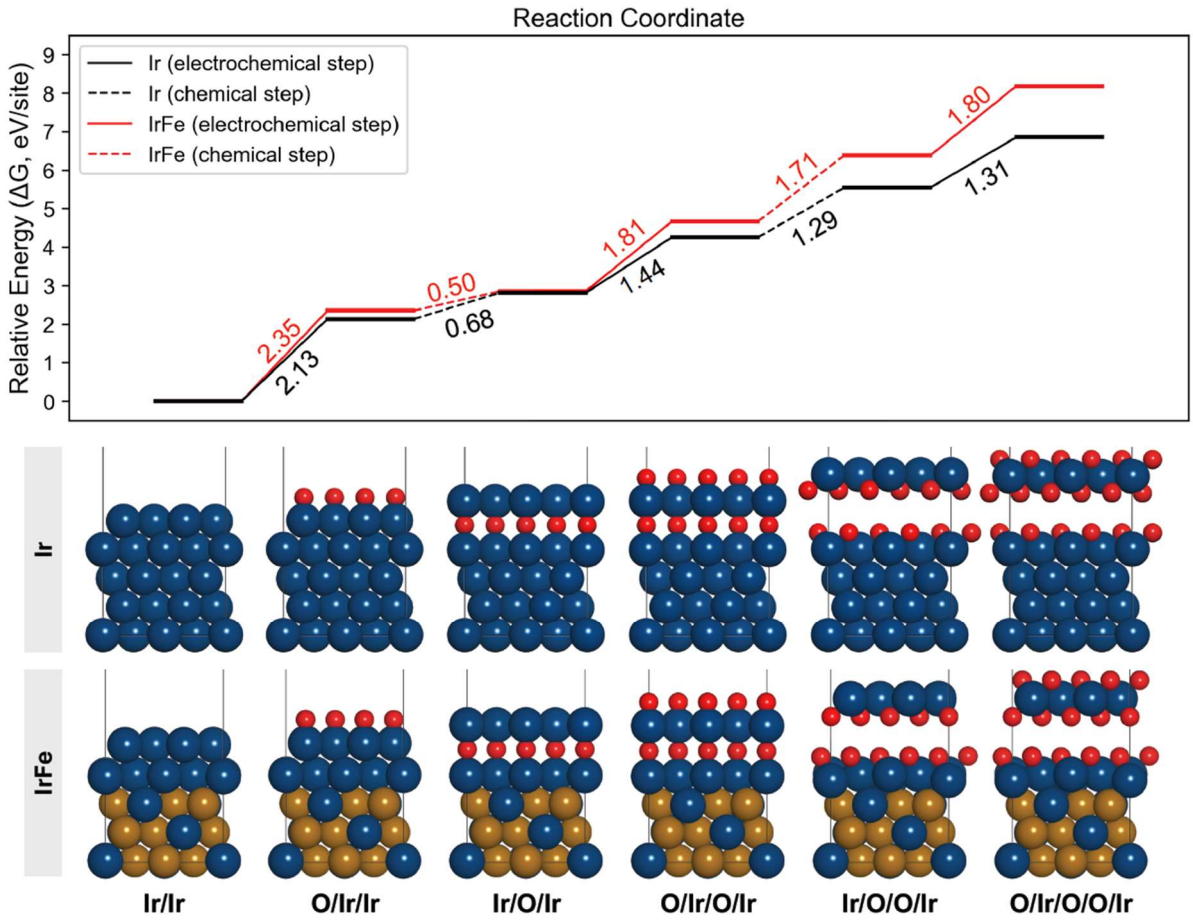

Figure S32. DFT-calculated energetics for progressive surface oxidation on Ir and IrFe surfaces, along with the corresponding structural models. Electrochemical oxidation steps (solid lines) and subsequent chemical oxygen penetration steps (dashed lines) are distinguished. The reaction pathway describes the gradual evolution from metallic Ir surface layers to configurations containing a surface IrO_2 layer and subsurface oxygen, representing progressive oxide-layer thickening.

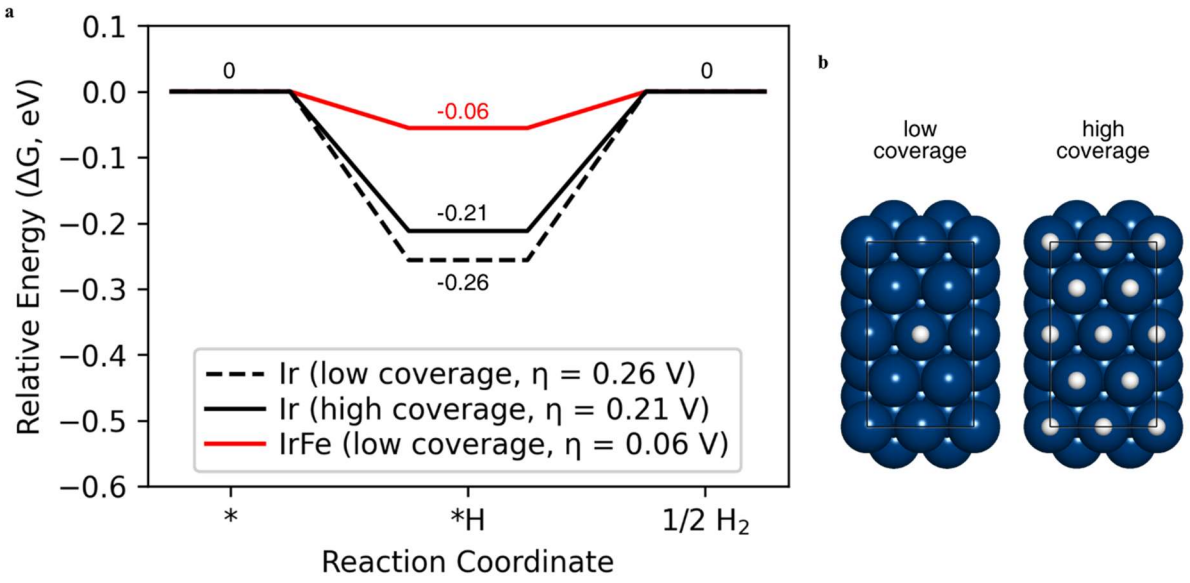

Figure S33. DFT-calculated HER energetics on Ir and IrFe surfaces. (a) DFT-calculated HER free energy diagrams and overpotentials (η) for Ir and IrFe surfaces. Computational Details for the complete stepwise reaction equations. **(b)** Top views of the corresponding HER intermediates on the Ir surface. Navy and white spheres represent Ir and H atoms, respectively.

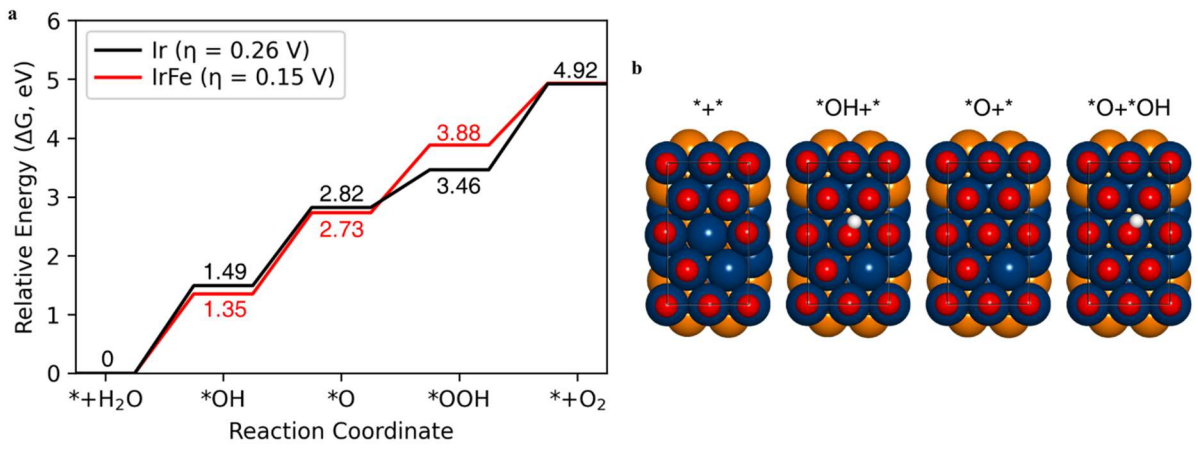

Figure S34. DFT-calculated OER energetics on Ir and IrFe surfaces. (a) DFT-calculated OER free energy diagrams and overpotentials (η) for Ir and IrFe surfaces. See Computational Details for the complete stepwise reaction equations. **(b)** Top views of the corresponding OER intermediates on the IrFe surface. Navy, orange, red, and white spheres represent Ir, Fe, O, and H atoms, respectively.

Full-Cell Performance Simulation and Degradation Mechanism Analysis

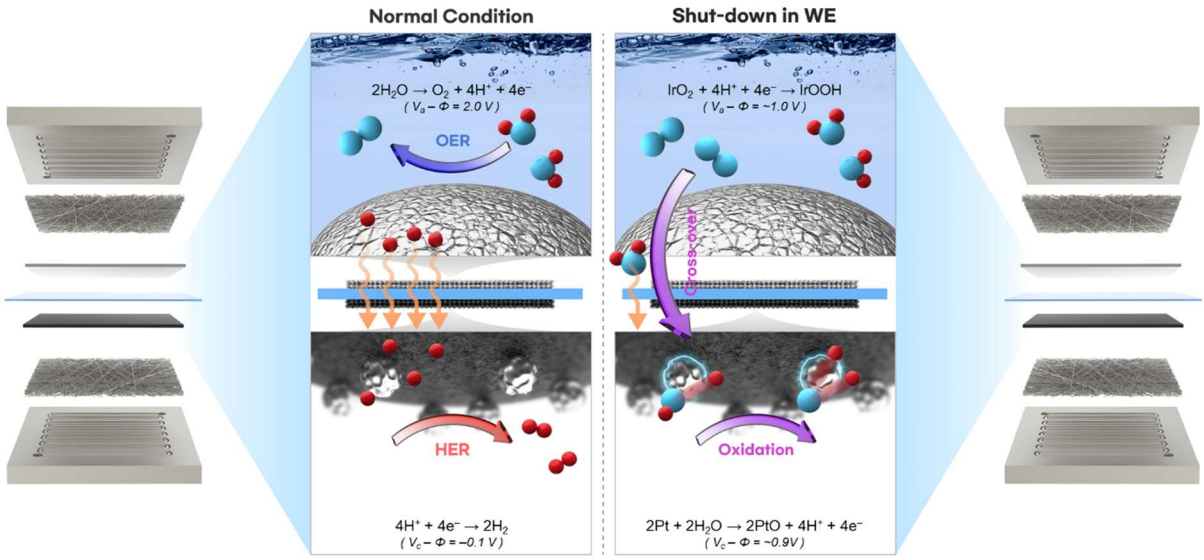

Figure S35. Electrode degradation mechanism during shutdown of proton exchange membrane water electrolyzer (PEMWE). The abrupt removal of external voltage causes a transient redistribution of charge within the membrane–electrode assembly. Residual ions and electronic imbalance can induce a reverse current, forcing the cathode to behave anodically. This inversion initiates unwanted oxidation reactions at the cathode, including oxygen evolution and potential catalyst dissolution, leading to the degradation of the active layer and reduced HER performance. The illustration depicts the electrochemical reaction pathway in normal condition and its implications for catalyst stability during shutdown transitions.

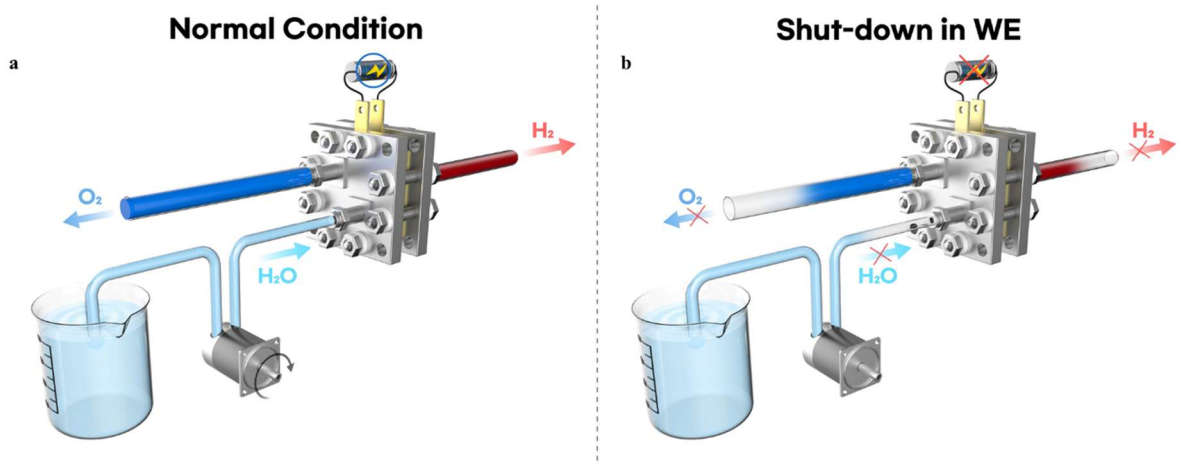

Figure S36. Testing protocol for simulation on WE Shutdown condition. (a) Normal operation and **(b)** Shutdown event.

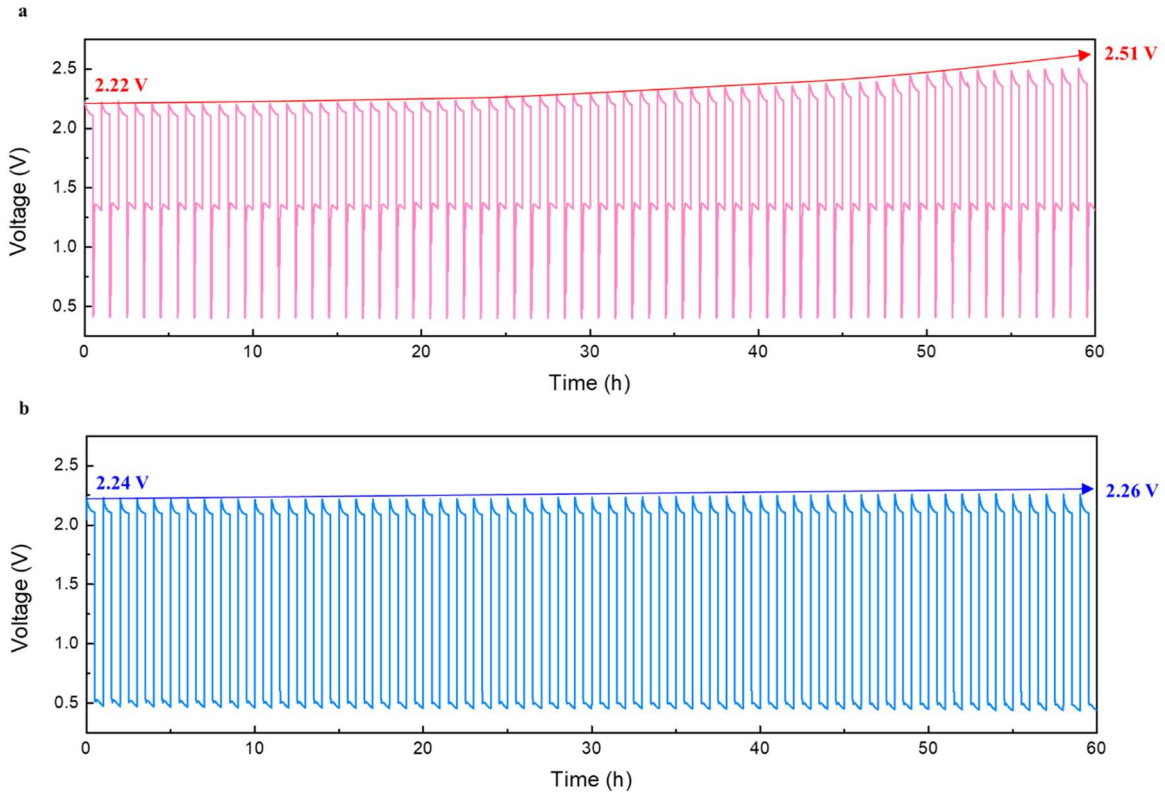

Figure S37. Variation of open-circuit voltage (OCV) during the shutdown protocol test. (a) Conventional MEA showing a stepwise increase in peak potential over the 60 h shutdown period, with transient voltage surges occurring at each cycle. **(b)** IrFe/C-based MEA at cathode of WE exhibiting a more stable potential profile, with suppressed peak growth and reduced fluctuation.

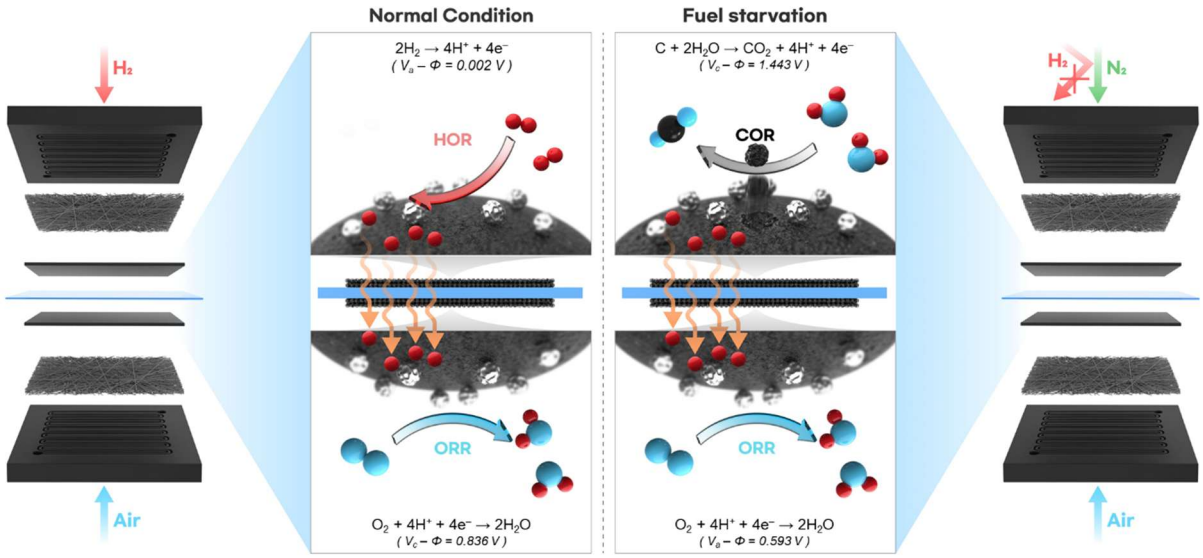

Figure S38. Electrode damage mechanism under fuel starvation in proton exchange membrane fuel cells (PEMFCs). During rapid acceleration, Insufficient hydrogen supply leads to fuel starvation, which gradually increases the anode potential. Water electrolysis via OER and carbon support corrosion via COR can competitively compensate for the lack of protons and electrons. However, due to the low OER activity of the Pt/C catalyst, when the anode potential exceeds 1.44 V, COR accelerates, leading to irreversible performance degradation of the carbon support and reduced fuel cell durability.

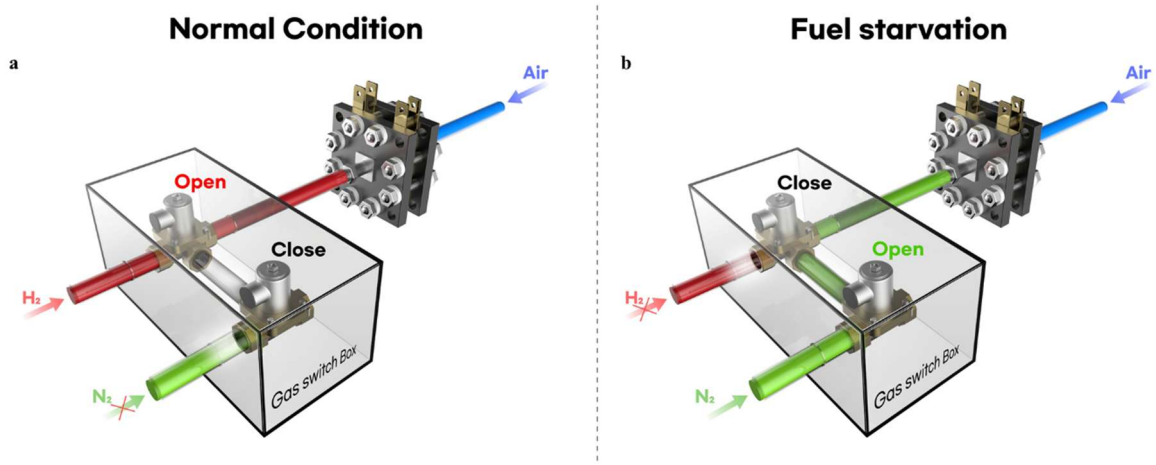

Figure S39. Testing protocol for simulation on fuel starvation condition. (a) Normal operation and **(b)** Fuel starvation event.

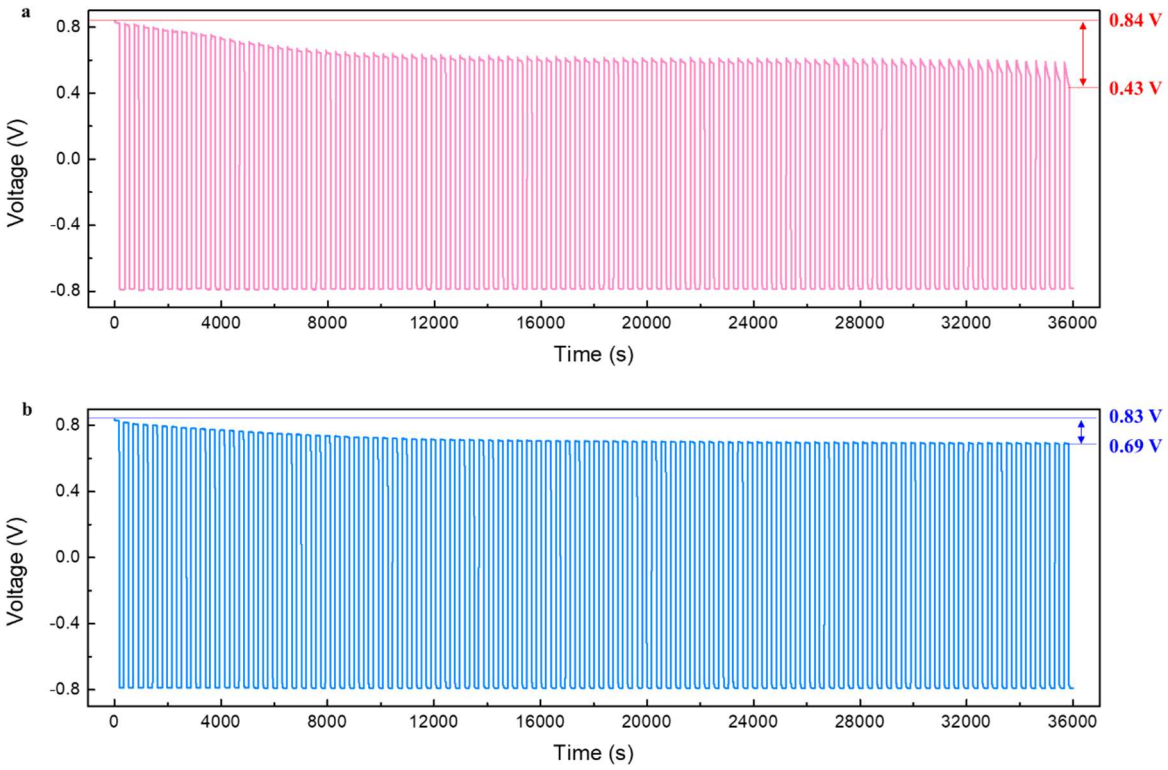

Figure S40. Potential profiling results during 10 h fuel starvation protocol for (a) conventional MEA and **(b)** IrFe/C-based MEA at anode of FC.

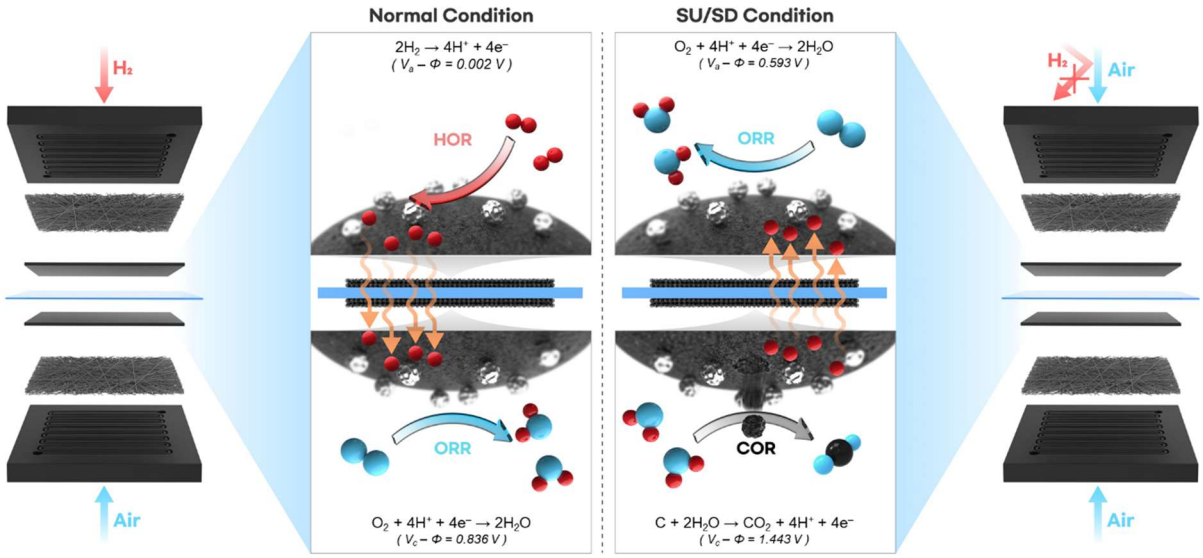

Figure S41. Schematic of electrochemical degradation mechanism during SU/SD events to the inner membrane electrode assembly of the PEMFC. Under normal operating conditions, hydrogen is supplied to the anode, and the cathode potential is regulated such that the OCV remains above 0.9 V. However, during SU/SD events, oxygen may diffuse into the anode, triggering the oxygen reduction reaction (ORR) at the anode side. This unintended ORR drives the cathode potential above 1.44 V, causing a sharp potential spike that accelerates carbon corrosion at the cathode. This mechanism is a major contributor to catalyst layer degradation and long-term performance loss in PEM fuel cells. Φ, electrolyte potential; V_a, anode metal potential; V_c, cathode metal potential.

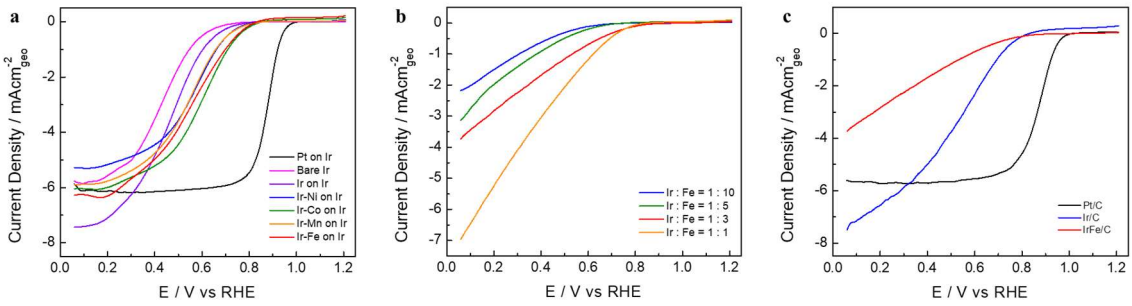

Figure S42. Evaluation of IrFe/C as a HOR-selective catalyst via oxygen reduction reaction (ORR) activity assessment in O_2-saturated 0.1 M $HClO_4$ at 1,600 rpm with a sweep rate of 10 mVs^{-1}. (a) Comparison of ORR activities across different Ir–TM/Ir model catalysts, **(b)** ORR polarization curves of IrFe/C with different Ir:Fe ratios, and **(c)** LSV curves for ORR of IrFe/C in stark contrast to commercial Pt/C and Ir/C catalysts.

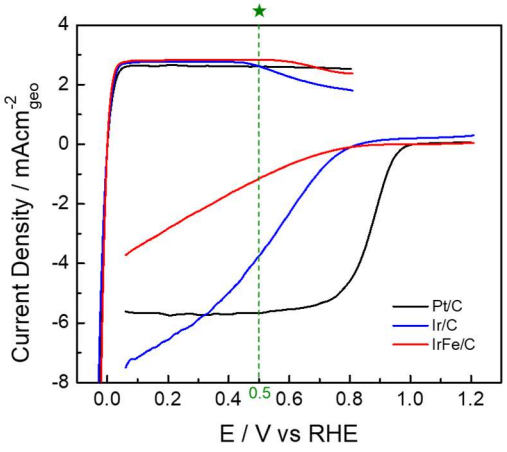

HOR Selectivity (@ 0.5 V vs RHE)			
	HOR (mA/cm^2)	ORR (mA/cm^2)	The ratio of HOR to ORR
Pt/C	2.64	−5.67	0.47
Ir/C	2.61	−3.76	0.69
IrFe/C	2.83	−1.14	2.48

Figure S43. Comparison of HOR and ORR polarization curves for Pt/C, Ir/C, and IrFe/C catalysts. The table summarizes the HOR selectivity (ratio of HOR to ORR current densities) evaluated at 0.5 V vs RHE.

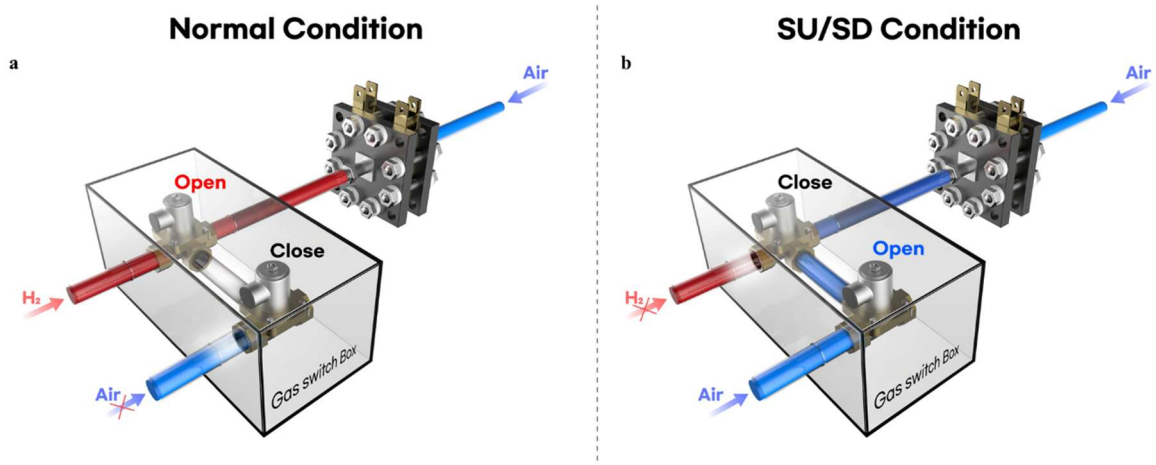

Figure S44. Testing protocol for simulation on SUSD condition. (a) Normal operation and **(b)** SU/SD event.

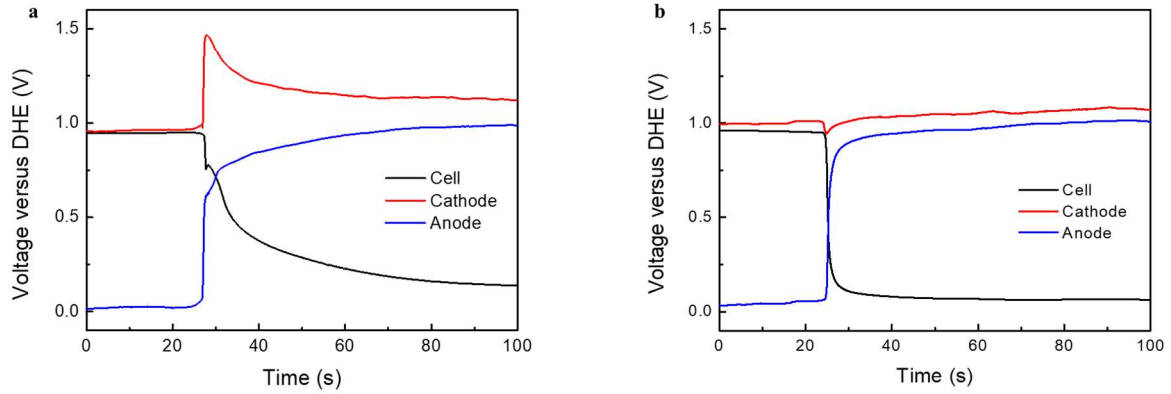

Figure S45. Direct measurement potential of cell and electrodes with DHE in SU/SD event for single cell containing (a) conventional MEA and **(b)** IrFe/C-based MEA at anode of FC.

Economic Viability Assessment of IrFe/C Catalyst

To assess the practical viability of the IrFe/C catalyst compared to commercial Pt/C, we performed a cost-effectiveness analysis based on the raw material loading and the average market prices of precious metals over the last 20 days (December 23, 2025 – January 11, 2026). Although Ir currently commands a higher market price than Pt, our strategy of alloying with non-precious Fe significantly reduces the specific Ir loading required, ensuring economic competitiveness.

1. Material Composition and Mass Fraction

The IrFe/C catalyst was synthesized with an optimal molar ratio of Ir:Fe=1:3. Based on the standard atomic weights (Ir: 192.22 g/mol, Fe: 55.85 g/mol), the mass fraction of Ir in the alloy nanoparticles is calculated as follows:

$$M_{IrFe} = (1 \times 192.22) + (3 \times 55.85) = 359.77\ g\ mol^{-1}$$

$$\text{Mass Fraction of Ir} = \frac{192.22}{359.77} \approx 0.534\ (53.4\ wt\%)$$

Consequently, approximately 46.6 wt% of the metallic mass consists of inexpensive Fe, which significantly dilutes the usage of precious Ir.

2. Specific Precious Metal Loading

For a rigorous comparison, both Pt/C and IrFe/C electrodes were prepared with the same total metal loading of $0.1\ mg_{metal}\ cm^{-2}$. The actual precious metal loading for each electrode is:

$$\text{Commercial Pt/C } (46.9\ wt\%\ Pt)\text{: } 0.1\ mg_{Pt}\ cm^{-2}$$

$$\text{IrFe/C } (40\ wt\%\ IrFe)\text{: } 0.1\ mg_{IrFe}\ cm^{-2} \times 0.534 = 0.0534\ mg_{Ir}\ cm^{-2}$$

By alloying with Fe, the required mass of Ir per unit area is reduced by approximately 47% compared to the Pt loading in the reference electrode.

3. Cost Calculation (Based on Market Prices)

We estimated the catalyst cost per geometric surface area using the average market prices of Pt and Ir for the recent 20-day period. *(Source: Johnson Matthey PGM Management, accessed January 11, 2026)*

$$\text{Average Price of Pt: } 2{,}251.58\ \text{USD}\ oz^{-1}\ (\approx 72.39\ USD\ g^{-1})$$

$$\text{Average Price of Ir: } 4{,}795.83\ \text{USD}\ oz^{-1}\ (\approx 154.19\ USD\ g^{-1})$$

The calculated costs are:

$$Cost_{Pt} = 0.1 \times 10^{-3}\ g\ cm^{-2} \times 72.39\ USD\ g^{-1} \approx 0.00724\ USD\ cm^{-2}$$

$$Cost_{Ir} = 0.0534 \times 10^{-3}\ g\ cm^{-2} \times 154.19\ USD\ g^{-1} \approx 0.00823\ USD\ cm^{-2}$$

4. Economic Feasibility and Total Cost of Ownership (TCO)

The calculation indicates that the raw material cost of the IrFe/C electrode is highly comparable to that of the Pt/C electrode (approx. 1.14 times). Despite the unit price of Ir being higher than Pt, the significant reduction in Ir loading via Fe alloying effectively offsets the cost difference. More importantly, considering the Total Cost of Ownership (TCO), the economic advantage of IrFe/C becomes evident. As demonstrated in this study, commercial Pt/C suffers from severe degradation (dissolution and oxidation) under transient conditions, necessitating frequent replacement. In contrast, IrFe/C exhibits exceptional intrinsic reversibility and durability under these harsh conditions. Therefore, the marginal difference in initial material cost is significantly outweighed by the extended operational lifetime and reduced system maintenance costs, verifying the practical economic viability of the IrFe/C catalyst.